Scientific Reports

https://doi.org/10.1038/s41598-026-45545-7

Article in Press

Magnetic amino-functionalized hyper-crosslinked resin as a reusable adsorbent for methylene blue

Received: 27 January 2026

Accepted: 19 March 2026

Published online: 25 March 2026

Cite this article as: Cirillo C., Iuliano M., Modestino M. *et al.* Magnetic amino-functionalized hyper-crosslinked resin as a reusable adsorbent for methylene blue. *Sci Rep* (2026). https://doi.org/10.1038/s41598-026-45545-7

Claudia Cirillo, Mariagrazia Iuliano, Michele Modestino, Armando Galluzzi, Federico Olivieri, Rachele Castaldo, Gennaro Gentile, Massimiliano Polichetti & Maria Sarno

Magnetic amino-functionalized hyper-crosslinked resin as a reusable adsorbent for methylene blue

Claudia Cirillo[a,b*], Mariagrazia Iuliano[a,b], Michele Modestino[a], Armando Galluzzi[a], Federico Olivieri[c], Rachele Castaldo[c], Gennaro Gentile[c], Massimiliano Polichetti[a,b], Maria Sarno[a, b]

[a]*Department of Physics "E.R. Caianiello", University of Salerno, Via Giovanni Paolo II, 132, 84084 Fisciano, SA, Italy*

[b]*Nano_Mates (Research Centre for Nanomaterials and Nanotechnology at the University of Salerno), University of Salerno, Via Giovanni Paolo II, 132, 84084 Fisciano, SA, Italy*

[c]*Institute for Polymers, Composites and Biomaterials, National Research Council of Italy, Via Campi Flegrei 34, Pozzuoli (NA), Italy*

ABSTRACT

Contamination of water resources by organic dyes is a major environmental issue associated with industrial activities. Methylene blue (MB), a widely used cationic aromatic dye, is particularly problematic due to its high chemical stability and toxicity, highlighting the need for efficient and cost-effective treatment strategies. In this study, a magnetic amino-functionalized hyper-crosslinked resin (Fe_3O_4@XDV-NH_2) was synthesized and evaluated as an efficient adsorbent for MB removal from aqueous solutions. The material was prepared via post-synthetic amino functionalization of a hyper-crosslinked polymer followed by in situ deposition of Fe_3O_4 nanoparticles, combining high surface area, permanent porosity, and chemical stability with easy magnetic separation. Structural and magnetic characterizations confirmed the uniform incorporation of Fe_3O_4 without significant loss of porosity. Amino functionalization enhanced hydrophilicity and introduced polar active sites, promoting strong interactions with MB. Batch adsorption experiments revealed a maximum adsorption capacity of 79.60 mg/g at 298 K and pH 9 and 0.06 g L^{-1} adsorbent dosage.

Adsorption kinetics followed the pseudo-second-order model (R^2 = 0.976). Equilibrium data were best fitted by the Langmuir isotherm model (R^2 = 0.996), indicating monolayer adsorption with a maximum theoretical capacity of 183.48 mg/g. Thermodynamic analysis showed that MB adsorption was spontaneous and exothermic. High removal efficiencies were maintained in complex matrices such as tap water (94.11%) and synthetic wastewater (78.41%). Moreover, the adsorbent retained approximately 89% of its initial capacity after six adsorption–desorption cycles, demonstrating good reusability. These results indicate that Fe_3O_4@XDV-NH_2 is a promising and sustainable adsorbent for dye-contaminated wastewater treatment.

Keywords: Fe_3O_4 nanoparticles; hyper-crosslinked polymer (HCP); magnetic separation; adsorption kinetics; adsorbent regeneration.

* Corresponding author: E-mail address: clcirillo@unisa.it (C.Cirillo). Tel.: +39 089 964335.

- Rachele: 0000-0002-4487-2287
- Federico: 0000-0002-1424-1257
- Gennaro: 0000-0002-1280-8926

1 Introduction

Dyes are chemical substances extensively employed as coloring agents in various industrial sectors, including textiles, paper, leather, printing, plastics, food, and cosmetics. These compounds, capable of modifying the color of materials, have become indispensable in numerous manufacturing processes [1,2]. According to the American Association of Textile Chemists and Colorists (AATCC) and the Society of Dyers and Colorists (SDC), more than 105 types of dyes are currently synthesized and commercially available worldwide. However, their widespread application has raised serious environmental concerns, particularly related to soil and water contamination. It is estimated that approximately 15% of the total global dye production is discharged into aquatic ecosystems [3,4]. Even at very low concentrations, these pollutants can significantly alter the color, transparency, and overall aesthetic quality of surface waters [5]. Aromatic organic dyes, such as methylene blue (MB), are particularly toxic and chemically stable compared to other classes of organic dyes. They can cause serious health effects in humans, including nausea, vomiting, tissue necrosis, and neurological damage [6]. Over the past few decades, numerous studies have explored physical, chemical, and biological approaches for treating dye-containing wastewater, including advanced oxidation processes, photocatalysis, reverse osmosis, coagulation/flocculation, biodegradation, and adsorption [7–17]. Although many of these methods demonstrate good removal efficiency, their high operational costs and complex handling procedures limit large-scale applications. Among the

available technologies, adsorption has emerged as one of the most efficient and economically viable methods owing to its simplicity, high removal efficiency, and the possibility of adsorbent regeneration and reuse [18,19]. The efficiency of the adsorption process depends on several operational parameters such as initial dye concentration, pH, adsorbent dosage, temperature, and contact time. For instance, pH influences the ionization of both dye molecules and the adsorbent surface, while temperature affects adsorption capacity and kinetics. The choice or synthesis of suitable adsorbents plays a fundamental role in the effectiveness of adsorption-based water treatment technologies [20]. Extensive literature surveys indicate that an ideal adsorbent should combine high adsorption capacity, rapid adsorption kinetics, selectivity toward target contaminants, chemical stability under water treatment conditions, large specific surface area, environmental compatibility, renewability, resistance to fouling, and feasibility for large-scale production [21-23]. To meet these requirements, a broad spectrum of adsorbent materials has been extensively developed, including activated carbon, carbon nanotubes, graphene and its derivatives, zeolites, metal–organic frameworks (MOFs), microgels, and adsorbents derived from agricultural and industrial wastes [24–30]. Beyond these conventional systems, considerable research efforts have focused on inorganic minerals, naturally derived polymers (such as chitosan, cellulose, and pectin), and synthetic polymeric materials (including polyacrylic acid and polyacrylamide) [31-34] . Among these materials, hyper-crosslinked polymers (HCPs) have emerged as a promising class of highly porous adsorbents due to their facile synthesis via Friedel–Crafts alkylation,

high surface area, tunable pore architecture, and excellent chemical stability, making them particularly effective for the removal of heavy metals and organic dyes from wastewater [35]. They offer numerous advantages, including mild synthesis conditions, low cost, high chemical and thermal stability, large Brunauer–Emmett–Teller (BET) specific surface area (SSA), and permanent porosity. Furthermore, HCPs exhibit strong affinity toward both polar and non-polar molecules, making them highly versatile materials [36-42]. Owing to these remarkable characteristics, HCPs have attracted considerable attention for a wide range of advanced applications, including environmental remediation, catalysis, energy storage, and molecular separation. They have been successfully applied in water purification, gas storage, supercapacitors, catalysis, drug delivery, and chromatographic separation [38-41]. However, its application for extracting aromatic compounds from aqueous solutions is limited due to its extreme hydrophobicity [42]. Therefore, for effective removal of target pollutants, it is of great interest to chemically modify the hyper-crosslinked resin to enhance its hydrophilic properties [43]. Chemical modification is a commonly employed method to alter the adsorption characteristics of adsorbents by surface modification or functionalization. Functionalization of HCPs is crucial to enhance their performance and selectivity in adsorption processes. The incorporation of heteroatoms such as nitrogen (N), oxygen (O), or sulfur (S) introduces surface heterogeneity and polar sites, which strengthen the interactions between the adsorbent and the target molecules. As reported by several authors [43-45], the introduction of amino groups significantly enhances adsorption capacity

and selectivity toward CO_2. It increases affinity toward polar organic dyes through polar interactions and toward metal cations through chelation. Such a functionalization increases the polarity of the polymer, also facilitating its localization in a specific phase of a system; for example, promoting its localization at the interface in emulsions designed to produce polymers templated within high internal phase emulsions (polyHIPEs) [46]. Moreover, functionalization with amino or other polar groups enhances the electronic properties of the polymer, such as dipole moment and polarizability, making it more suitable for the selective adsorption of polar molecules, even at low concentration. Post-synthetic modification is often preferred, as it allows precise control of surface chemistry without compromising the porous structure of the material. As highlighted in recent studies, functionalized HCPs have shown excellent adsorption capacity, chemical stability, and selectivity for the removal of organic dyes from aqueous solutions [46-49]. Nevertheless, despite their high efficiency, the recovery and separation of these materials after use remain challenging, limiting their large-scale applicability. The separation of nanosized adsorbents often involves time-consuming and inefficient steps, reducing the overall process's practicality. To overcome this limitation, the introduction of magnetic functionalities enables rapid and efficient separation under an external magnetic field. Magnetic nanoparticles (MNPs) [50], particularly magnetite (Fe_3O_4), have demonstrated excellent biocompatibility, stability, and low cost. Magnetic composites can be easily recovered and reused, improving overall process efficiency and sustainability. In this study, we hypothesize that an amino-functionalized magnetic hyper-

crosslinked resin (Fe_3O_4@XDV-NH_2), can be effectively designed for the efficient removal of methylene blue (MB) from aqueous solutions. The material is expected to combine the high surface area, adsorption capacity, and chemical stability of hyper-crosslinked polymers with the easy magnetic separation provided by Fe_3O_4 nanoparticles, enabling rapid recovery and reuse. Furthermore, the introduction of amino functional groups is expected to enhance interactions with MB molecules and maintain high adsorption performance even in complex water matrices such as tap water and synthetic wastewater.

2 Materials and Methods

Hyper-crosslinked resins were synthesized and functionalized to introduce amino groups (XDV–NH_2) following the procedure previously reported in Ref. [44]. The synthesis of XDV–NH_2 is schematically illustrated in Figure 1a and consists of three sequential stages. First, vinyl benzyl chloride (VBC) and divinyl benzene (DVB) undergo free-radical polymerization under a nitrogen atmosphere, using AIBN as an initiator, yielding a crosslinked polymeric precursor (i). Subsequently, hyper-crosslinking is carried out via a Friedel–Crafts reaction catalyzed by ferric chloride ($FeCl_3$) in dichloroethane, leading to the formation of a rigid and highly microporous network (ii). Finally, functionalization is performed through a two-step process: nitration with a mixed acid solution and reduction of the nitro groups to amino functionalities using stannous chloride ($SnCl_2$) in an acidic medium, resulting in the aminated material XDV–NH_2 (iii). The obtained XDV–NH_2 was then further

modified by incorporation of Fe_3O_4 nanoparticles to produce the magnetic composite Fe_3O_4@XDV–NH_2, as shown in Figure 1b. Adsorption tests with methylene blue (MB) were carried out in batch mode, and recyclability was evaluated through desorption experiments with different solvents. The materials were characterized using electron microscopy, spectroscopic analyses, and magnetic measurements. A full description of the experimental protocols is reported in the Supplementary Materials.

3 Results and discussion

3.1 Morphology characterization

The hyper-crosslinked resin XDV-NH_2 is a highly microporous material, exhibiting a Langmuir specific surface area of 1190 ± 20 $m^2\ g^{-1}$ and a total pore volume of 0.36 $cm^3\ g^{-1}$, with micropores accounting for 72% of the overall porosity [44]. After magnetic modification, the Fe_3O_4@XDV-NH_2 composite shows a reduced specific surface area (851 ± 18 $m^2\ g^{-1}$), which can be attributed to the incorporation of Fe_3O_4 nanoparticles that introduce a non-porous mass fraction and partially occupy the pore structure. Nevertheless, the material retains a significant portion of its porosity, indicating that the hyper-crosslinked framework is largely preserved during magnetization. The high specific surface area of XDV-NH_2 arises from the rigid and extensively crosslinked network generated via Friedel–Crafts alkylation, which produces a permanent microporous structure with a large accessible internal surface area [45]. Such a prominent microporous character is particularly significant, as it provides a high density of accessible

adsorption sites and greatly enhances the material's capacity for capturing organic pollutants and metal cations from aqueous solutions. [46,52-54]. SEM images of XDV-NH_2 and Fe_3O_4@XDV-NH_2 are illustrated in Figure 2. The morphology of XDV-NH_2 (Figure 2a) shows compact and uniformly distributed structures, confirming the homogeneity of the raw material. At high magnification (inset of Figure 2a), the SEM images reveal a rough surface and a porous internal structure. After iron precipitation, the morphology changes significantly. Figures 2b–d of the Fe_3O_4@XDV-NH_2 sample show the presence of some iron oxide agglomerates, although they are relatively small, both on the surface and in the interparticle regions; overall, however, the distribution appears controlled and consistent with a uniform deposition of Fe_3O_4. The SEM images reveal the presence of aggregates domains of Fe_3O_4 nanoparticles exhibiting predominantly sub-spherical to slightly irregular morphologies and generally well distributed within the polymer matrix. These domains correspond to clusters of nanoparticles rather than isolated individual particles, with characteristic sizes ranging from 200 to 500 nm. EDX analysis and elemental mapping further validate the successful iron precipitation process. The EDX spectrum of Fe_3O_4@XDV-NH_2 confirms the presence of C, N, O, and Fe, while the corresponding elemental maps (Figure 3a and 3b) demonstrate a homogeneous distribution of these elements. The iron signal is evenly dispersed and well-integrated with those of carbon, nitrogen, and oxygen, confirming the effective anchoring of Fe_3O_4 nanoparticles onto the XDV-NH_2 matrix.

3.2 XRD studies

Figure 4a reports the XRD patterns of the XDV-NH_2 and Fe_3O_4@XDV-NH_2 samples. For the XDV-NH_2 sample (blue profile), no well-defined peaks at 2θ are observed, and the diffractogram appears rather noisy, which is typical of amorphous materials, where no long-range crystalline order is present. In contrast, the XRD pattern of the Fe_3O_4@XDV-NH_2 sample (red profile) clearly shows the characteristic peaks of magnetite, located at 2θ = 30.54° (220), 35.62° (311), 43.29° (400), 53.57° (422), 57.23° (511), and 62.84° (440) [55-57]. These signals are in full agreement with the values reported in the literature and successfully confirm the effective incorporation of the magnetic nanoparticles within the amino resin matrix. The average crystallite size of the Fe_3O_4 nanoparticles present in the sample was estimated using the Scherrer equation [58, 59] applied to the peak corresponding to the (311) plane, yielding a value of approximately 8.0 ± 2 nm. This size clearly falls within the nanometric range. It is consistent with the values commonly reported for magnetite nanoparticles synthesized by similar methods [60,61].

3.3 FT-IR analysis

The FT-IR spectra of the XDV-NH_2 and Fe_3O_4@XDV-NH_2 samples are shown in Figure 4b. For the XDV-NH_2 sample, the spectrum exhibits characteristic bands confirming the presence of the main organic functionalities of the resin: the bands at 2923 cm^{-1} and 2859 cm^{-1}, assigned to the asymmetric and symmetric stretching of –CH_2 groups [62], respectively; and an intense band at 1599 cm^{-1}, corresponding to the bending vibrations of the –NH_2 group. In addition, the band at 3373 cm^{-1} can be attributed to N–H stretching, in agreement with literature

data [62,63]. Moreover, the aromatic and aliphatic C-N absorption bands at 1286 cm^{-1} and 1089 cm^{-1} [64,65]. These signals confirm the successful amino functionalization of the polymeric matrix. In the case of Fe_3O_4@XDV-NH_2, besides the bands already observed for the organic support, a significant variation is detected in the low-frequency region: the signal at around 546 cm^{-1}, attributed to C–H out-of-plane vibrations of substituted aromatic rings [66], shifts to 528 cm^{-1} after Fe_3O_4 incorporation, which can be assigned to the stretching vibration of the Fe–O bond, confirming the presence of magnetite in the composite [67-69]. This shift provides direct evidence of the formation of magnetite nanoparticles and their effective incorporation within the amino resin matrix. Moreover, the absorption band at 1089 cm^{-1} is not observed in the Fe_3O_4@XDV-NH_2, likely due to the high intensity of the Fe–O stretching vibration, which overlaps and dominates this region of the spectrum and the possibility of the coordination interactions between amine groups and iron oxide nanoparticles. Generally, the results obtained from both SEM-EDX, XRD, and FT-IR analyses clearly demonstrate the successful incorporation of magnetite nanoparticles and the effective magnetization of the Fe_3O_4@XDV-NH_2 sample. Figure S1 presents the thermogravimetric (TG) profiles of the amino hyper-cross-linked resin (XDV-NH_2) and the magnetic amino hyper-cross-linked resin (Fe_3O_4@XDV-NH_2). The TG curve of XDV-NH_2 shows an initial weight loss attributed to the removal of physically adsorbed moisture, followed by a second major weight loss in the temperature range of 230–600 °C, corresponding to the complete degradation of the polymeric support. In contrast, Fe_3O_4@XDV-NH_2 exhibits a residual weight of

approximately 13% at high temperatures. This residual mass is attributed to the magnetite (Fe_3O_4) content within the resin. Moreover, the presence of the inorganic magnetic phase appears to promote and slightly accelerate the thermal degradation of the polymeric matrix in the nanocomposite.

3.4 M(H) and M(T) measurements

Magnetization versus magnetic field measurements, M(H), were carried out at 5 K and 300 K for both samples. The measurements were performed by increasing the field from 0 Oe to 90,000 Oe, decreasing it to –90,000 Oe, and then returning to 90,000 Oe, taking particular care to reduce the trapped field in the magnet before each run [70]. The results at 300 K are reported in Figure 5a. In it is possible to see that the XDV-NH_2 sample has no relevant magnetic signal compared to the Fe_3O_4@XDV-NH_2 one. Due to this, only the characterization performed on the Fe_3O_4@XDV-NH_2 sample has been shown. In Figure 5b, a clear reduction of the coercive field with increasing temperature is observed for the Fe_3O_4@XDV-NH_2 sample: at 5 K, it shows a coercive field (H_c) of 550 Oe, while at 300 K, the H_c is reduced to 16 Oe. The magnetization at 90 kOe also decreases from about 11 emu/g at 5 K to 8.6 emu/g at 300 K. This reduction in coercivity and magnetization is expected for a transition to the superparamagnetic state [71,72]. However, the value of H_c = 16 Oe, different from 0 Oe, indicates that not all nanoparticles are superparamagnetic at this temperature. Furthermore, the magnetization at 90 kOe does not correspond to the expected value for Fe_3O_4 nanoparticles [73], since the normalization mass includes both the resin (non-magnetic) and the nanoparticles. A

magnetization versus temperature measurement, M(T), was also performed between 5 K and 300 K on the Fe_3O_4@XDV-NH_2 sample. After zeroing the field, the temperature was reduced to 5 K; then a field of 100 Oe was applied, and the magnetization was measured by heating up to 300 K (Zero Field Cooling curve, ZFC) and cooling back down to 5 K (Field Cooling curve, FC). The result is shown in Figure 5c. The ZFC curve displays a maximum at 87 K, which can be considered the average blocking temperature (T_B) of the sample [74,75]. The lack of overlap between ZFC and FC curves across the whole temperature range indicates a broad distribution of T_B, related to a wide nanoparticle size distribution. An initial overlap is observed only at temperatures below 300 K. This behavior is consistent with the M(H) measurements, where the decrease in coercivity at 300 K is attributed to the transition of nanoparticles to an unblocked state [72]. To further investigate this transition, the temperature derivative of the difference between the ZFC and FC curves was analyzed [74, 75]. The result, reported in Figure 5d, shows a monomodal distribution with a maximum at about 21 K. Fitting the curve with a lognormal function, which is the expected distribution for T_B due to the nanoparticle size distribution, yielded the following parameters: distribution center 28.6 K and log standard deviation 0.68. The large value of the standard deviation is consistent with previous observations and confirms a broad nanoparticle size distribution [74].

3.5 Zeta potential investigation

The Zeta potential of Fe_3O_4@XDV-NH_2 samples was measured in the pH range 2–10 using a STABINO ZETA analyzer. At pH values below

5.5, the samples displayed a positive surface charge due to the protonation of amino groups, thereby enhancing the electrostatic adsorption of anionic dyes. Conversely, at pH values above 5.5, the surface became negatively charged, favouring interactions with cationic species (see Figure S2).

3.6 Optimization of the process parameters

3.6.1 Effect of time and pH

A crucial parameter regulating the adsorption process of MB is the solution pH, as it simultaneously affects the ionization state of the dye molecules and the surface charge distribution of the adsorbent. In this study, the adsorption behavior of MB was investigated at three representative pH values (3, 6, and 9), with the process monitored for up to 60 minutes. As shown in Figure S3, the UV-Vis spectra reveal a gradual decrease in the characteristic absorption band of MB with increasing contact time, confirming the progressive reduction of dye concentration in solution due to adsorption. The quantitative results presented in Figures 6a and 6b demonstrate that the residual amount of MB (expressed in mg) decreased continuously over time at all tested pH values, with a particularly enhanced removal efficiency at pH 9. After 60 min, the residual MB concentration was 2.54 mg at pH 3 (49.2% removal; adsorption capacity 82.0 mg/g), 2.37 mg at pH 6 (58.6% removal; 87.8 mg/g), and as low as 1.71 mg at pH 9 (65.8% removal; maximum capacity 109.7 mg/g).

This behavior can be explained by considering both the isoelectric point (pH_{pzc}) of the adsorbent and the ionization properties of MB. Being a cationic dye, MB remains positively charged across the

studied pH range [76,77]. At pH values lower than the pH_{pzc}, the surface of the adsorbent is predominantly positively charged due to protonation of functional groups, which leads to electrostatic repulsion with MB cations, thereby limiting the adsorption efficiency. Consistently, zeta potential measurements of Fe_3O_4@XDV-NH_2 show positive surface charge values below pH 5.5, confirming the protonation of amino groups (–NH_2 to –NH_3^+) and supporting the electrostatic repulsion observed at pH 3. In contrast, when the pH exceeds the pH_{pzc}, surface deprotonation occurs, and the adsorbent becomes negatively charged, establishing strong electrostatic attractions with MB cations. Accordingly, the zeta potential becomes negative above pH 5.5, clearly indicating the formation of a negatively charged interface. This electrostatic transition explains the marked decrease in residual concentration and the enhanced adsorption capacity observed at pH 9. Therefore, alkaline conditions (pH 9) were identified as the most favorable not only for adsorption kinetics but also for achieving the maximum adsorption capacity, whereas at pH 3 and 6, the efficiency was limited by electrostatic repulsion. Based on these results, subsequent adsorption experiments were conducted at pH 9, which was determined to be the optimal condition for MB removal.

3.6.2 Effect of adsorbent concentration

The influence of adsorbent dosage on the removal of MB was investigated under optimal conditions (pH = 9, initial MB concentration = 5 mg/L, temperature = 25 °C, and agitation speed =

220 rpm), varying the amount of adsorbent between 0.03 and 0.07 g/L. The results clearly demonstrate that the removal efficiency (%) increases markedly with increasing dosage, particularly during the early stages of the process when the availability of active sites plays a crucial role in capturing MB molecules. As shown in Figure 7a, a sharp decrease in MB concentration occurs within the first 10–20 minutes, followed by a more gradual decline until a plateau is reached, indicating the progressive saturation of surface-active sites. In contrast, the adsorption capacity (Figure 7b), expressed as mg of MB adsorbed per gram of adsorbent, exhibits an opposite trend: it is higher at lower dosages but decreases with increasing dosage. This behavior is typical of adsorption systems, as at higher dosages the relative number of available adsorption sites exceeds the amount of MB molecules in solutions, resulting in incomplete site utilization. Thus, higher dosages enhance overall removal but reduce the normalized adsorption capacity. The UV–Vis spectra presented in Figure 7c illustrate the temporal evolution of MB removal for the dosage of 0.06 g/L. A progressive decrease in the intensity of the characteristic MB absorption peak is observed with contact time, confirming the steady reduction of dye concentration in solution. Similarly, the photograph in Figure 7d, also obtained at 0.06 g/L, provides clear visual evidence of this process: the initially intense blue solution gradually fades over 60 minutes, directly reflecting the progressive removal of MB molecules.

The increase in adsorbent dosage from 0.03 to 0.06 g/L significantly enhances the removal efficiency; however, further increasing the

dosage to 0.07 g/L results in only a marginal improvement (see Figure 7a). This finding suggests that above 0.06 g/L, the adsorbent mass is no longer a limiting factor, as the concentration of MB in solution becomes insufficient to take full advantage of the additional sites. Therefore, 0.06 g/L can be considered the optimal dosage, ensuring high removal efficiency while avoiding unnecessary excess of adsorbent.

3.6.3 Effect of temperature

In Figure 8, the results of MB adsorption at pH 9 under optimal operating conditions are presented at three different temperatures: 298 K, 308 K, and 318 K. The analysis clearly shows that temperature has a significant influence on the performance of the adsorbent. At 298 K, the best performance is achieved, both in terms of removal efficiency (Figure 8a) and adsorption capacity (Figure 8b). Under these conditions, the interaction between the cationic MB molecules and the negatively charged active sites of the adsorbent is more favorable, resulting in an increased amount of dye absorbed per unit mass of material. Conversely, as the temperature increases (308 K and especially 318 K), a progressive decrease in performance is observed. The removal efficiency tends to decline, and the adsorption capacity decreases proportionally, indicating that at higher temperatures, thermal energy counteracts the attractive electrostatic interactions between MB and the adsorbent surface. 298 K represents the most favorable condition to maximize both the overall removal of MB and the specific adsorption capacity of the material.

3.6.4 Effect of MB concentration

The adsorption capacity of an adsorbent is strongly influenced by the initial dye concentration. Generally, the removal efficiency tends to decrease with increasing initial dye concentration when the active sites on the adsorbent surface approach saturation. However, the adsorption capacity usually increases with higher initial concentrations due to the greater driving force for mass transfer. The effect of the initial dye concentration was investigated at different contact times (0–60 min) for initial concentrations of 5, 10, 20, and 30 mg/L (see Figure S4). The experimental results indicate that the removal efficiency varies significantly with increasing initial concentration. At the lowest concentration (5 mg/L), the removal efficiency increased rapidly with contact time, reaching about 96.0% after 60 min, while the adsorption capacity reached 79.6 mg/g. When the initial concentration increased to 10 mg/L, the removal efficiency after 60 min slightly decreased to 89.7% (see Figure S4), whereas the adsorption capacity increased significantly to 149.5 mg/g. A further increase in the initial concentration to 30 mg/L resulted in a more pronounced decrease in removal efficiency. These results indicate that the percentage removal decreases with increasing initial dye concentration, which can be attributed to the limited number of active adsorption sites available on the adsorbent surface. At higher concentrations, these sites become saturated more rapidly, thereby reducing the overall removal efficiency (see Figure S4). Nevertheless, the adsorption capacity increases with increasing initial concentration, owing to the higher concentration gradient that enhances the mass transfer of dye molecules from the solution to the adsorbent surface.

3.7 Adsorption kinetics

To gain deeper insight into the adsorption dynamics of MB onto Fe_3O_4@XDV-NH_2, the kinetic behaviour was investigated at pH 9 with an adsorbent dosage of 0.06 g/L. The experimental data were evaluated by fitting them to two commonly applied kinetic models: Lagergren's pseudo-first order and the pseudo-second-order model [78].

The equation of pseudo-first order was defined as:

$$\ln(q_e - q_t) = \ln(q_e) - k_1 t \qquad (1)$$

where q_e and q_t (mg/g) are the equilibrium MB amount and the time t (min) MB adsorbed quantity, while k_1 is the constant of adsorption (min^{-1}).

The equation of pseudo-second order was defined as:

$$\frac{t}{q_t} = \frac{1}{k_2 q_e^2} - \frac{1}{k_2} t \qquad (2)$$

with: q_e and q_t (mg/g), the equilibrium and at the t time (min) amounts of MB adsorbed, respectively, while the constant of adsorption (min g mg^{-1}) is k_2. The experimental kinetic data for the adsorption of MB onto Fe_3O_4@XDV-NH_2 at pH 9 and 0.06 g/L were analysed using Lagergren's pseudo-first order and pseudo-second-order models, as shown in Figure S5a and S5b, respectively. The fitting parameters are reported in Table S1. For the pseudo-first-order model, the calculated equilibrium adsorption capacity ($q_{e,cal}$) was 59.80 mg/g, with a rate constant (k_1) of 0.052 min^{-1} and a correlation coefficient (R^2) of 0.845. Although this model could partially describe the adsorption trend, the relatively low R^2 indicates that it does not adequately fit the experimental data. On the other hand, the pseudo-second-order model provided a much better

description of the kinetic process. The calculated adsorption capacity ($q_{e,cal}$) was 92.07 mg/g, with a rate constant (k_2) of 0.00985 g $mg^{-1}min^{-1}$ and a higher correlation coefficient (R^2 = 0.976). Although the model slightly overestimates the experimental equilibrium adsorption capacity ($q_{e,exp}$ = 79.60 mg g^{-1}), it provides the best fit to the kinetic data. The regression analysis indicates that the pseudo-second-order model most appropriately describes the adsorption kinetics of MB onto Fe_3O_4@XDV-NH_2. However, this kinetic model should not be interpreted as direct evidence of chemisorption. Rather, it suggests that the adsorption rate is governed by the availability of active sites and by adsorbate–adsorbent interactions [79-81]. A similar kinetic trend has been reported for the adsorption of methylene blue onto papaya bark fiber, where the pseudo-second-order model was also found to provide the best fit [82,83], suggesting that the interaction between the dye and the active sites represents the rate-controlling step. The adsorption process was analyzed using the Weber intraparticle diffusion model (see Figure S5c):

$$q_t = k_d t^{1/2} + c \quad (3)$$

where k_d(mg g^{-1} $min^{-1/2}$) is the intraparticle diffusion rate constant and c(mg/g) represents the intercept related to the boundary layer effect. In this study, only one linear region was observed, corresponding to the initial stage of adsorption onto the resin (Figure S4c). Since the line does not pass through the origin, intraparticle diffusion is not the sole rate-controlling step. The intercept value suggests that external mass

transfer to the resin surface significantly influences the adsorption process [84].

3.8 Adsorption isotherm

The interaction of polluting dye molecules with the active sites on the adsorbent surface was described by adsorption isotherm models. Furthermore, it is employed to examine the correlation between the mass of the ingested adsorbent and the quantity of pollutant absorbed at equilibrium conditions. In this particular investigation, dye concentrations between 5 and 30 mg/L were considered, with the other three parameters, adsorbent dose of 0.06 g/L, solution pH of 9, and contact period of 60 min, being maintained at their optimal levels. The analysis of data fitness and the determination of the homogeneity or heterogeneity of the adsorbent surfaces were conducted using the Langmuir and the Freundlich isotherms (see Figure S6a and S6b). The Langmuir equilibrium isotherm model postulates a monolayer distribution of dye at specific homogeneous sites within the adsorbent surface, with no interaction between adsorbed species. The following equation represents a linearized form of the Langmuir model:

$$\frac{C_e}{q_e} = \frac{1}{q_{max} K_L} + \frac{C_e}{q_{max}} \qquad (4)$$

Here, q_{max} (mg/g) denotes the maximum adsorption capacity at monolayer coverage, and K_L (L/mg) is the Langmuir constant parameter associated with the energy of adsorption and affinity of binding sites between adsorbate and adsorbent. A linear plot of C_e/q_e versus C_e was observed (Figure S6a). The values of q_{max} (mg/g), K_L (L/mg), and correlation coefficient (R^2) were determined from the plot and are

provided in Table S2. The Freundlich isotherm model was applied to heterogeneous surface systems. Its linear form is represented as:

$$\mathrm{LN}\,Q_E = \mathrm{LN}\,K_F + \frac{1}{N}\mathrm{LN}\,C_E \qquad (5)$$

where K_f is the Freundlich constant, which relates to the capacity of the adsorbent for the adsorbate, and 1/n is the heterogeneity factor associated with the intensity of adsorption. The values of K_f, n, and the correlation coefficient (R^2) are determined through linear regression plotting in Figure S6b. For favorable adsorption, the value of n should fall between 1 and 10 [85]. The adsorption parameters are listed in Table S2. Based on the obtained results, the experimental data fit better with the Langmuir isotherm model, which showed the highest coefficient of determination (R^2 = 0.996). Figure S5a shows a linear relationship between specific adsorption (Ce/qe) and equilibrium concentration (Ce) with a coefficient of correlation (R^2) of 0.996, confirming the applicability of the Langmuir model to demonstrate the homogenous nature of Fe_3O_4@XDV-NH_2, as an adsorbent, i.e. equal amount of adsorption activation energy is associated with each dye molecule. The maximum monolayer capacity q_{max} for MB onto Fe_3O_4@XDV-NH_2, obtained from the Langmuir model, is 183.48 mg/g at 25℃. The R^2 value appears to indicate that the Freundlich isotherm model is less suited when compared with the Langmuir isotherm model.

3.9 Adsorption thermodynamics

Thermodynamic parameters, namely, free energy, enthalpy, and entropy changes of adsorption, were estimated using Vant Hoff's equation [86] (see Figure S7). In this study, the thermodynamic behaviour of MB

adsorption onto the adsorbent was investigated at different temperatures (298, 308, and 318 K). As reported in Table S3, the Gibbs free energy change (ΔG°) values were negative at all tested temperatures, ranging from –14.55 kJ/mol at 298 K to –8.69 kJ/mol at 318 K. These results confirm that the adsorption of MB is a spontaneous process at room temperature [87]. However, the progressive decrease in the absolute value of ΔG° with increasing temperature indicates that spontaneity tends to diminish as the system is subjected to higher thermal energy. The enthalpy change (ΔH°) was calculated as −101.7 kJ/mol, suggesting that the adsorption of MB is an exothermic process. The decrease in adsorption capacity observed with increasing temperature can be attributed to the rise in thermal energy of the system, which counteracts the attractive interactions between MB molecules and the active sites of the adsorbent. This behaviour suggests that, once adsorbed, MB molecules tend to adopt a more ordered configuration on the adsorbent surface. Furthermore, the increase in temperature enhances the mobility and solubility of MB in the aqueous phase, as well as the kinetic energy of the species involved, thereby promoting the desorption of MB molecules and weakening the adsorbent–adsorbate interactions [88-91], consistent with strong interactions and the alignment of the cationic dye molecules onto the negatively charged active sites.

3.10 Adsorption in real water systems

To better approximate realistic operating conditions, additional adsorption experiments were carried out using MB solutions prepared

in two different aqueous matrices: tap water (Fisciano, Italy) and synthetic wastewater. Owing to the limited availability of accessible industrial discharge sites in the Salerno area, the wastewater samples were artificially formulated to contain MB (5 mg/L), CH_3COONa (500 mg/L), NaCl (200 mg/L), KCl (200 mg/L), $CaCl_2$ (200 mg/L), KSCN (500 mg/L), $(NH_4)_2SO_4$ (150 mg/L), and phenol (10 mg/L); the concentration of metal ions (Fe, Cu, Zn, and Mn) was maintained below 10 µg/L [92]. This approach enabled a preliminary assessment of the influence of naturally occurring ionic species as well as coexisting organic and inorganic contaminants on the adsorption performance of the material. To ensure consistency and comparability, the experimental setup and operating parameters were kept identical to those used in experiments conducted with deionized water. The adsorption behavior of Fe_3O_4@XDV-NH_2 toward MB under realistic aqueous matrices is shown in Figure S8. In tap water, Fe_3O_4@XDV-NH_2 exhibits high adsorption performance, achieving a removal efficiency of 94.11% after 60 min, indicating good resistance to interference from commonly occurring ions. In contrast, experiments conducted in synthetic wastewater show a moderate decrease in adsorption efficiency compared to deionized water and tap water systems. This reduction can be attributed to competitive adsorption by coexisting contaminants, particularly as phenol and ionic species, as well as to the effects of the complex wastewater matrix on the surface properties of the adsorbent. However, a removal efficiency of approximately 78.41% is still achieved after 60 min, highlighting the promising performance of the material under challenging, real-water conditions.

3.11 Adsorption mechanism

The structure of Fe_3O_4@XDV-NH_2, characterized by the presence of amino and hydroxyl groups as well as aromatic domains rich in π-electrons, exhibits both hydrophilic–hydrophobic features and a partially mesoporous architecture. These characteristics suggest that the adsorption of MB is governed by multiple interactions, including hydrophobic interaction, electrostatic attraction, π–π interactions, pore-filling effects, and hydrogen bonding. The role of surface functional groups was clarified through FT-IR analyses performed before and after adsorption (Figure S9a). Before adsorption, the FT-IR spectrum of Fe_3O_4@XDV-NH_2 shows the presence of several surface functional groups. After the adsorption of methylene blue, the FT-IR spectrum of the modified material exhibits noticeable variations in the intensity of the bands, while their positions remain almost unchanged. In particular, the vibrational band due to aromatic C=C bond of Fe_3O_4@XDV-NH_2 + MB shifted from 1659 to 1636 cm^{-1}, which could be due to localization of aromatic π-electrons of Fe_3O_4@XDV-NH_2 owing to the π-π bond interactions of aromatic rings of both MB and Fe_3O_4@XDV-NH_2 molecules. Additionally, the intensity of N-H stretching vibrations of Fe_3O_4@XDV-NH_2 around 3373 cm^{-1} in Fe_3O_4@XDV-NH_2 + MB increased abruptly. This indicates the H-bonding between the nitrogen atom of MB and the H-atom of amine groups (Fe_3O_4@XDV-NH_2) [93]. These observations indicate that the adsorption of MB onto Fe_3O_4@XDV-NH_2 mainly involves non-covalent interactions rather than the formation of new covalent chemical bonds. The changes in band intensity can be attributed to the formation of non-covalent interactions,

including hydrogen bonding, hydrophobic interactions, and electrostatic forces, between the methylene blue molecules and the functional groups present on the surface of Fe_3O_4@XDV-NH_2. Combined with the kinetic analysis, these results indicate that the adsorption process is governed by surface interactions and by the accessibility of active sites rather than by the formation of strong chemical bonds. In particular, the decrease or variation in the intensity of certain absorption bands suggests that the dye molecules have been incorporated or entrapped within the matrix of the material, occupying the available active sites. The results indicate that the adsorption of MB onto Fe_3O_4@XDV-NH_2 proceeds through a synergistic mechanism, in which electrostatic attractions between the cationic dye and the negatively charged surface are combined with hydrogen bonding, hydrophobic interactions, π–π interactions, and pore-filling effects. In particular, the –NH_2 groups play a key role in promoting the capture of MB molecules (see Figure S9b).

3.12 Desorption & reusability investigation

Since the interaction between MB and the Fe_3O_4@XDV-NH_2 adsorbent is quite strong, solvent treatment alone is not sufficient to rapidly induce the desorption of the MB molecule interacting with the adsorbent surface. For this reason, desorption was investigated using different solvents under controlled conditions (contact time: 120 min; T = 25 °C). As shown in Figure 9a, among the solvents tested (HCl, ethanol, acetone, propanol, and water), the HCl solution exhibited the highest desorption efficiency, reaching approximately 90% for MB. This result can be attributed to the high concentration of H_3O^+ ions, which protonate the

adsorbent surface and enhance the electrostatic repulsion between cationic MB molecules and the functional groups of Fe_3O_4@XDV-NH_2, thereby promoting dye release. The reusability of Fe_3O_4@XDV-NH_2 was further evaluated through seven successive adsorption–desorption cycles. Adsorption was carried out under optimal conditions (pH = 9; adsorbent dose = 0.06 g/L; initial MB concentration = 5 mg/L; agitation speed = 220 rpm), followed by desorption with HCl (contact time: 120 min; T = 25 °C). As reported in Figure 9b, adsorption efficiency gradually decreased from 100% in the first cycle to 89% in the sixth cycle. The observed decline in adsorption efficiency can be attributed to the partial saturation of active sites and possible modifications of the adsorbent surface during repeated use and following the chemical regeneration process, as well as to slight physical and chemical structural alterations of the Fe_3O_4@XDV-NH_2 material [94]. Despite this slight decrease in performance, the results indicate that Fe_3O_4@XDV-NH_2 exhibits good recyclability and can be considered a promising adsorbent for the treatment of NPs-contaminated wastewater, while maintaining good chemical and structural stability even after repeated adsorption–desorption cycles.

3.13 Comparison with literature

Various magnetic hybrid nanocomposite materials have been employed as adsorbents for dye removal from contaminated water. Table 1 summarizes the adsorption performances of different magnetic hybrids [95-100], allowing a direct comparison between the results of this study and those reported in the literature. The Fe_3O_4@XDV-NH_2

nanocomposites synthesized in this work achieved an adsorption capacity of 79.60 mg g^{-1} for methylene blue (MB) under the investigated experimental conditions. Although this value is lower than that reported for some adsorbents, such as NH_2-MWCNTs@Fe_3O_4 (178.5 mg/g) [99] and AO-Fe-SWCNTs(256.69 mg/g) [98], it is higher than that of ACSO/Fe_3O_4 (60.60 mg/g) [100], MGC-4 (65.79 mg/g) [95] magnetized corn cob (13.23 mg/g) [96]. Therefore, Fe_3O_4@XDV-NH_2 exhibits competitive adsorption performance, particularly in terms of capacity. Importantly, the developed nanocomposite also demonstrates good reusability, retaining high removal efficiency over multiple adsorption–desorption cycles. This cyclic stability, combined with the contribution of multiple interaction mechanisms (electrostatic interactions, π–π interactions, and hydrophobic bonding) and the advantage of facile magnetic separation, positions Fe_3O_4@XDV-NH_2 as a promising candidate for dye removal applications, especially where rapid adsorption and repeated use under moderate operating conditions are required.

4 Conclusion

An amino-functionalized magnetic hyper-crosslinked resin (Fe_3O_4@XDV-NH_2) was successfully synthesized and demonstrated high efficiency in methylene blue adsorption. The structural analyses confirmed the homogeneous dispersion of Fe_3O_4 nanoparticles and the stability of the polymeric matrix, while the magnetic measurements showed a superparamagnetic behavior. The adsorption process was optimized under alkaline conditions (pH 9) and room temperature, following a

pseudo-second-order kinetic model. Thermodynamic parameters indicated a spontaneous and exothermic process governed by electrostatic attraction and π–π interactions. The material exhibited excellent reusability, with an adsorption efficiency of over 89% remaining after six consecutive adsorption–desorption cycles. Fe_3O_4@XDV-NH_2 combines high adsorption capacity, magnetic recoverability, and stability, making it a promising candidate for efficient dye removal and sustainable wastewater treatment applications.

Acknowledgement

Rachele Castaldo acknowledges financial support under the Italian Science Fund (FIS 2 Call) funded by the Italian Ministry of University and Research (MUR) for the project *HIerarchically Porous materials with tailored ADsorption properties to face environmental pollution* (HIPAD, Proposal code FIS-2023-01686, CUP B53C24009520001, Grant Assignment Decree No. n. 23314 adopted on 11/12/2024 by the Italian MUR).

Data Availability: The datasets used and/or analysed during the current study available from the corresponding author on reasonable request

Authors' contributions: C.C.: Conceptualization; Data Curation; Formal analysis; Investigation; Methodology; Validation; Visualization; Writing - Original Draft; Writing - Review & Editing; Supervision. **M.I**., Conceptualization; Data Curation; Formal analysis; Investigation; Methodology; Validation; Visualization; Writing - Original Draft; Writing - Review & Editing. **M.M.; A.C.:** Data Curation; Conceptualization; Investigation; Methodology. Investigation, Writing - Original Draft. **F.O.; R.C:** Investigation; Writing - Original Draft; Visualization. **G.G.; M.P.; M.S.:** Supervision; Validation; Writing - Original Draft; Writing - Review & Editing.

Funding: The authors have not disclosed any funding.

Declarations Conflict of Interest: There is no conflict of interest in this research

References

[1]. Jorge, A. M., Athira, K., Alves, M. B., Gardas, R. L., & Pereira, J. F. (2023). Textile dyes effluents: A current scenario and the use of aqueous biphasic systems for the recovery of dyes. Journal of Water Process Engineering, 55, 104125. https://doi.org/10.1016/j.jwpe.2023.104125

[2]. Fröse, A., Schmidtke, K., Sukmann, T., Junger, I. J., & Ehrmann, A. (2018). Application of natural dyes on diverse textile materials. Optik, 181, 215–219. https://doi.org/10.1016/j.ijleo.2018.12.099

[3]. Zollinger, H. (1987). Color Chemistry: Synthesis, Properties, and Applications of Organic Dyes and Pigments (pp. 92–100). VCH Publishers.

[4]. Kayranli, B. (2011). Adsorption of textile dyes onto iron-base waterworks sludge from aqueous solution: Isotherm, kinetic and thermodynamic study. Chemical Engineering Journal, 173, 782–791. https://doi.org/10.1016/j.cej.2011.08.051

[5]. Hunger, K. (2003). Industrial Dyes: Chemistry, Properties, Applications. Wiley-VCH. https://doi.org/10.1002/3527602011

[6]. Karri, R. R., Ravindran, G., & Dehghani, M. H. (2021). Wastewater—Sources, toxicity, and their consequences to human health. In R. R. Karri et al. (Eds.), Soft Computing Techniques in Solid Waste and Wastewater Management (pp. 3–33). https://doi.org/10.1016/B978-0-12-824463-0.00001-X

[7]. Buitrón, G., Quezada, M., & Moreno, G. (2003). Aerobic degradation of the azo dye acid red 151 in a sequencing batch

biofilter. Bioresource Technology, 92, 143–149. https://doi.org/10.1016/j.biortech.2003.09.001

[8]. Muthuraman, G., & Teng, T. T. (2009). Extraction of methyl red from industrial wastewater using xylene as an extractant. Progress in Natural Science, 19, 1215–1220. https://doi.org/10.1016/j.pnsc.2009.04.002

[9]. Badr, Y., El-Wahed, M. A., & Mahmoud, M. A. (2008). Photocatalytic degradation of methyl red dye by silica nanoparticles. Journal of Hazardous Materials, 154, 245–253. https://doi.org/10.1016/j.jhazmat.2007.10.020

[10]. Ercan, Ö., Deniz, S., Yetimoğlu, E. K., & Aydın, A. (2015). Degradation of reactive dyes using advanced oxidation method. Clean: Soil, Air, Water, 43, 1031–1036. https://doi.org/10.1002/clen.201400195

[11]. Duta, A., & Visa, M. (2015). Simultaneous removal of two industrial dyes by adsorption and photocatalysis on a fly-ash–TiO_2 composite. Journal of Photochemistry and Photobiology A: Chemistry, 306, 21–30. https://doi.org/10.1016/j.jphotochem.2015.03.007

[12]. Boumaza, S., Kaouah, F., Omeiri, S., Trari, M., & Bendjama, Z. (2015). Removal of dyes by an integrated process coupling adsorption and photocatalysis in batch mode. Research on Chemical Intermediates, 41, 2353–2375. https://doi.org/10.1007/s11164-013-1351-5

[13]. Nataraj, S., Hosamani, K., & Aminabhavi, T. (2009). Nanofiltration and reverse osmosis thin film composite membrane module for the removal of dye and salts from the simulated mixtures. Desalination, 249, 12–17. https://doi.org/10.1016/j.desal.2009.06.008

[14]. Anjanyeulu, Y., Sreedhara Chary, N., & Suman Raj, D. S. (2005). Decolourization of industrial effluents – available methods and emerging technologies – A review. Reviews in Environmental Science and Biotechnology, 4, 245–273. https://doi.org/10.1007/s11157-005-1246-z

[15]. Vikrant, K., Giri, B. S., Raza, N., Roy, K., Kim, K.-H., Rai, B. N., & Singh, R. S. (2018). Recent advancements in bioremediation of dye: Current status and challenges. Bioresource Technology, 253, 355–367. https://doi.org/10.1016/j.biortech.2018.01.029

[16]. Legerská, B., Chmelová, D., & Ondrejovič, M. (2018). Decolourization and detoxification of monoazo dyes by laccase from the white-rot fungus Trametes versicolor. Journal of Biotechnology, 285, 84–90. https://doi.org/10.1016/j.jbiotec.2018.08.011

[17]. Rani, B., Kumar, V., Singh, J., Bisht, S., Teotia, P., Sharma, S., & Kela, R. (2014). Bioremediation of dyes by fungi isolated from contaminated dye effluent sites for bio-usability. Brazilian Journal of Microbiology, 45, 1055–1063. https://doi.org/10.1590/s1517-83822014000300039

[18]. Chebli, D., Fourcade, F., Brosillon, S., Nacef, S., & Amrane, A. (2010). Supported photocatalysis as a pre-treatment before biological degradation for the removal of some dyes from aqueous solutions: Acid red 183, Biebrich Scarlet, methyl red sodium salt, and orange II. Journal of Chemical Technology and Biotechnology, 85, 555–563.https://doi.org/10.1002/jctb.2342

[19]. Manjunatha, A. S., Sukhdev, A., & Puttaswamy. (2013). Oxidative decolorization of methyl red dye with chloramine-T kinetic and mechanistic chemistry. Indian Journal of Chemical Technology, 20, 416–422.

[20]. Ighalo, J. O., Rangabhashiyam, S., Dulta, K., Umeh, C. T., Iwuozor, K. O., Aniagor, C. O., Eshiemogie, S. O., Iwuchukwu, F. U., & Igwegbe, C. A. (2022). Recent advances in hydrochar application for the adsorptive removal of wastewater pollutants. Process Safety and Environmental Protection, 184, 419–456. https://doi.org/10.1016/j.cherd.2022.06.028

[21]. Gkika, D. A., Mitropoulos, A. C., & Kyzas, G. Z. (2022). Why reuse spent adsorbents? The latest challenges and limitations. The Science of the Total Environment, 822, 153612. https://doi.org/10.1016/j.scitotenv.2022.153612

[22]. Sajid, M. (2022). Chitosan-based adsorbents for analytical sample preparation and removal of pollutants from aqueous media: Progress, challenges and outlook. Trends in Environmental Analytical Chemistry, 36, e00185. https://doi.org/10.1016/j.teac.2022.e00185

[23]. Younas, F., Mustafa, A., Farooqi, Z. U. R., Wang, X., Younas, S., Mohy-Ud-Din, W., Hameed, M. A., Abrar, M. M., Maitlo, A. A., Noreen, S., & Hussain, M. M. (2021). Current and emerging adsorbent technologies for wastewater treatment: trends, limitations, and environmental implications. Water, 13(2), 215. https://doi.org/10.3390/w13020215

[24]. Bhatnagar, A., Hogland, W., Marques, M., & Sillanpää, M. (2012). An overview of the modification methods of activated carbon for its water treatment applications. Chemical Engineering Journal, 219, 499–511. https://doi.org/10.1016/j.cej.2012.12.038

[25]. Peng, J., He, Y., Zhou, C., Su, S., & Lai, B. (2020). The carbon nanotubes-based materials and their applications for organic pollutant removal: A critical review. Chinese Chemical Letters, 32(5), 1626–1636. https://doi.org/10.1016/j.cclet.2020.10.026

[26]. Sodha, V., Shahabuddin, S., Gaur, R., Ahmad, I., Bandyopadhyay, R., & Sridewi, N. (2022). Comprehensive Review on Zeolite-Based Nanocomposites for Treatment of Effluents from Wastewater. Nanomaterials, 12(18), 3199. https://doi.org/10.3390/nano12183199

[27]. Rout, D. R., Jena, H. M., Baigenzhenov, O., & Hosseini-Bandegharaei, A. (2022). Graphene-based materials for effective adsorption of organic and inorganic pollutants: A critical and comprehensive review. The Science of the Total Environment, 863, 160871. https://doi.org/10.1016/j.scitotenv.2022.160871

[28]. Abdollahi, N., Moussavi, G., & Giannakis, S. (2022). A review of heavy metals' removal from aqueous matrices by Metal-Organic

Frameworks (MOFs): State-of-the art and recent advances. Journal of Environmental Chemical Engineering, 10(3), 107394. https://doi.org/10.1016/j.jece.2022.107394

[29]. Naseem, K., Arif, M., Anwar, A., Haider, S., & Akhtar, M. S. (2023). Investigating adsorptive potential of Raphanus caudatus leaves biomass for methyl orange dye: isotherm and kinetic study. Zeitschrift Für Physikalische Chemie, 237(8), 1183–1205. https://doi.org/10.1515/zpch-2023-0255

[30]. Juela, D. M. (2021). Promising adsorptive materials derived from agricultural and industrial wastes for antibiotic removal: A comprehensive review. Separation and Purification Technology, 284, 120286. https://doi.org/10.1016/j.seppur.2021.120286

[31]. Mosaffa, E., Malekshah, R. E., Chavez, F. A., & Banerjee, A. (2025). Biogenic chitosan cross-linked cherry gum and N-doped biochar beads: An eco-friendly platform for versatile dual-site dye removal. International Journal of Biological Macromolecules, 339(Pt 2), 150037. https://doi.org/10.1016/j.ijbiomac.2025.150037

[32]. Mosaffa, Elias., Patel R.I, Purohit, A. M., Basak, B. B. Banerjee, A. (2023). Efficient Decontamination of Cationic Dyes from Synthetic Textile Wastewater Using Poly(acrylic acid) Composite Containing Amino Functionalized Biochar: A Mechanism Kinetic and Isotherm Study. J Polym Environ 31, 2486–2503 (2023). https://doi.org/10.1007/s10924-022-02744-3

[33]. Mosaffa, E., Jamshidi, E., Malekshah, R. E., Chakraborty, D., Oroujzadeh, M., Chavez, F. A., Ghafuri, H., & Banerjee, A. (2025). Physiochemically cross-linked cherry gum–LDH@Biochar

chitosan/PVA biosorbent for antibiotic removal: Monte Carlo and mechanistic insights. Desalination, 619, 119545. https://doi.org/10.1016/j.desal.2025.119545

[34]. Mosaffa, E., Patel, D., Ramsheh, N. A., Patel, R. I., Banerjee, A., & Ghafuri, H. (2023). Bacterial cellulose microfiber reinforced hollow chitosan beads decorated with cross-linked melamine plates for the removal of the Congo red. International Journal of Biological Macromolecules, 254(Pt 2), 127794. https://doi.org/10.1016/j.ijbiomac.2023.127794

[35]. Fontanals, N., Marcé, R. M., Borrull, F., & Cormack, P. A. G. (2015). Hyper-crosslinked materials: Preparation, characterisation and applications. Polymer Chemistry, 6(41), 7231–7244. https://doi.org/10.1039/c5py00771b

[36]. Abid, A., Razzaque, S., Hussain, I., & Tan, B. (2021). Eco-friendly phosphorus and nitrogen-rich inorganic–organic hybrid hypercross-linked porous polymers via a low-cost strategy. Macromolecules, 54(12), 5848–5855. https://doi.org/10.1021/acs.macromol.1c00385

[37]. Wang, R., Luan, X., Yaseen, M., Bao, J., Li, J., Zhao, Z., & Zhao, Z. (2023). Swellable array strategy based on designed flexible double hypercross-linked polymers for synergistic adsorption of toluene and formaldehyde. Environmental Science & Technology, 57(16), 6682–6694. https://doi.org/10.1021/acs.est.3c00565

[38]. Shi, P., Chen, X., Sun, Z., Li, C., Xu, Z., Jiang, X., & Jiang, B. (2019). Thickness controllable Hyper-crosslinked porous polymer

nanofilm with high CO_2 capture capacity. Journal of Colloid and Interface Science, 563, 272–280. https://doi.org/10.1016/j.jcis.2019.12.038

[39]. Hubert, O., Todorovic, N., González, L. M. R., Costagliola, E., Blocher, A., Mautner, A., Woodward, R. T., & Bismarck, A. (2023). Sulfonated Hyper-crosslinked polymer enhanced structural composite supercapacitors. Composites Science and Technology, 242, 110152. https://doi.org/10.1016/j.compscitech.2023.110152

[40]. Dong, Y., Zhou, Z., Wang, Y., Li, X., Li, T., Ren, Y., Hu, W., Zhang, L., Zhang, X., & Wei, C. (2022). Palladium supported on pyrrole functionalized Hyper-crosslinked polymer: Synthesis and its catalytic evaluations towards Suzuki–Miyaura coupling reactions in aqueous media. Journal of Molecular Liquids, 368, 120679. https://doi.org/10.1016/j.molliq.2022.120679

[41]. Razzaque, S., Cheng, Y., Hussain, I., & Tan, B. (2020). Synthesis of surface functionalized hollow microporous organic capsules for doxorubicin delivery to cancer cells. Polymer Chemistry, 11(12), 2110–2118. https://doi.org/10.1039/c9py01772k

[42]. Wang, X., Li, G., Guo, D., Zhang, Y., & Huang, J. (2016). A novel polar-modified post-cross-linked resin and its enhanced adsorption to salicylic acid: Equilibrium, kinetics and breakthrough studies. Journal of Colloid and Interface Science, 470, 1–9. https://doi.org/10.1016/j.jcis.2016.02.046

[43]. Moradi, M. R., Torkashvand, A., Penchah, H. R., & Ghaemi, A. (2023). Amine functionalized benzene-based Hyper-crosslinked

polymer as an adsorbent for CO_2/N_2 adsorption. Scientific Reports, 13(1). https://doi.org/10.1038/s41598-023-36434-4

[44]. Castaldo, R., Avolio, R., Cocca, M., Errico, M. E., Avella, M., & Gentile, G. (2021). Amino-functionalized hyper-crosslinked resins for enhanced adsorption of carbon dioxide and polar dyes. Chemical Engineering Journal, 418, 129463. https://doi.org/10.1016/j.cej.2021.129463

[45]. Huang, J., & Turner, S. R. (2017). Hypercrosslinked Polymers: a review. *Polymer Reviews*, *58*(1), 1–41. https://doi.org/10.1080/15583724.2017.1344703

[46]. Burevska-Atkovska, K., Olivieri, F., Avolio, R., Castaldo, R., Cocca, M., Errico, M. E., Gentile, G., & Grozdanov, A. (2024). Amino-modified microporous hyper-crosslinked resins for heavy metal ions adsorption. Colloids and Surfaces a Physicochemical and Engineering Aspects, 700, 134720. https://doi.org/10.1016/j.colsurfa.2024.134720

[47]. Castaldo, R., Berezovska, I., Silverstein, M. S., & Gentile, G. (2023). PolyHIPEs Containing Hyper-Cross-Linked Resins: Hierarchical Porosity with Broad and Versatile Sorption Properties. ACS Applied Polymer Materials, 5(9), 6920–6931. https://doi.org/10.1021/acsapm.3c00974

[48]. Zhu, Y., Ding, R., Chen, S., Qu, X., Yang, Y., & Zhang, X. (2023). Three-dimensional sulfonic-functionalized porphyrin-based porous organic polymer for high-performance methylene blue and ciprofloxacin capture. Separation and Purification

Technology, 333, 125857. https://doi.org/10.1016/j.seppur.2023.125857

[49]. Zhang, X., Li, S., Wang, Y., Shen, J., Wei, Y., & Wang, C. (2025). Preparation of amino/hydroxy dual-functionalized Hyper-crosslinked polymers for effective removal of organic dyes from water. Journal of Hazardous Materials, 488, 137405. https://doi.org/10.1016/j.jhazmat.2025.137405

[50]. You, X., Han, L., & Liu, Q. (2023). Adsorption of Rhodamine B from aqueous solutions using polarity-tunable hyper-cross-linked resins. New Journal of Chemistry, 47(32), 15250–15260. https://doi.org/10.1039/d3nj02711b

[51]. Bushra, R., Ahmad, M., Alam, K., Seidi, F., Qurtulen, N., Shakeel, S., Song, J., Jin, Y., & Xiao, H. (2024). Recent advances in magnetic nanoparticles: Key applications, environmental insights, and future strategies. Sustainable Materials and Technologies, 40, e00985. https://doi.org/10.1016/j.susmat.2024.e00985

[52]. Maglione, A., Olivieri, F., Avolio, R., Castaldo, R., Cocca, M., Errico, M. E., Ambrogi, V., & Gentile, G. (2025). Hyper-Cross-linked Cellulose Nanofibrils with Spontaneous and Reversible Adsorption of Aromatic Pollutants from Water as a Valid Alternative to Fossil-Based Adsorbents. ACS Applied Materials & Interfaces, 17(26), 38619–38634. https://doi.org/10.1021/acsami.5c05009

[53]. Cirillo, C., Iuliano, M., Funicello, N., Castaldo, R., Avolio, R., Errico, M. E., Gentile, G., De Pasquale, S., Romano, P., & Sarno, M. (2025). Magnetic resonance imaging monitoring of 4-

chlorophenol removal by an efficient Horseradish Peroxidase-modified hyper-cross-linked resin catalyst. Journal of Environmental Chemical Engineering, 13(3), 116650. https://doi.org/10.1016/j.jece.2025.116650

[54]. Guerritore, M., Olivieri, F., Avolio, R., Castaldo, R., Cocca, M., Errico, M. E., Lavorgna, M., Silvestri, B., Ambrogi, V., & Gentile, G. (2022). Hierarchical micro-to-macroporous silica nanoparticles obtained by their grafting with hyper-crosslinked resin. Microporous and Mesoporous Materials, 335, 111864. https://doi.org/10.1016/j.micromeso.2022.111864

[55]. Dirgayanti, D. S., Koesnarpadi, S., & Hindryawati, N. (2021). Synthesis and characterization of Fe_3O_4-activated carbon and its application to adsorb methylene blue. IOP Conference Series: Earth and Environmental Science, 623(1), 012070. https://doi.org/10.1088/1755-1315/623/1/012070

[56]. Iuliano, M., Ponticorvo, E., Cirillo, C., & Sarno, M. (2022). A new nanocomposite from Vesuvian slope pinecones for azo-dyes removal. Industrial & Engineering Chemistry Research, 61(5), 1965–1976. https://doi.org/10.1021/acs.iecr.1c03574

[57]. Chen, F., Xie, S., Huang, X., & Qiu, X. (2016). Ionothermal synthesis of Fe3O4 magnetic nanoparticles as efficient heterogeneous Fenton-like catalysts for degradation of organic pollutants with H2O2. Journal of Hazardous Materials, 322(Pt A), 152–162. https://doi.org/10.1016/j.jhazmat.2016.02.073

[58]. Iuliano, M., Ponticorvo, E., Cirillo, C., Castaldo, R., De Pasquale, S., Gentile, G., & Sarno, M. (2023). Wax esters from

waste fish oil catalysed by immobilized Candida rugosa lipase. Process Biochemistry, 130, 386–400. https://doi.org/10.1016/j.procbio.2023.04.028

[59]. Shi, M., Tang, W., Guo, S., & Chen, F. (2025). Construction of hierarchically porous α-Fe2O3 nanosheets from Fe-PVP hybrid gel for sustainable Fenton-like degradation of tetracycline antibiotics with low H2O2 consumption. *Environmental Research*, *286*(Pt 2), 122854. https://doi.org/10.1016/j.envres.2025.122854

[60]. Fecková, M., Tóth, J., Šálek, P., Španová, A., Horák, D., Shubhra, Q. T. H., Kovařík, A., Gyenis, J., & Rittich, B. (2021). Capture of DNAs by magnetic Hyper-crosslinked poly(styrene-co-divinylbenzene) microspheres. Journal of Materials Science, 56(9), 5817–5829. https://doi.org/10.1007/s10853-020-05649-5

[61]. Cirillo, C., Iuliano, M., Funicello, N., Castaldo, R., Avolio, R., Errico, M. E., Gentile, G., De Pasquale, S., Romano, P., & Sarno, M. (2025). Magnetic resonance imaging monitoring of 4-chlorophenol removal by an efficient horseradish peroxidase-modified hyper-cross-linked resin catalyst. Journal of Environmental Chemical Engineering, 116650. https://doi.org/10.1016/j.jece.2025.116650

[62]. Zhang, W., Du, Q., Pan, B., Lv, L., Hong, C., Jiang, Z., & Kong, D. (2009). Adsorption equilibrium and heat of phenol onto aminated polymeric resins from aqueous solution. Colloids and Surfaces A: Physicochemical and Engineering Aspects, 346(1–3), 34–38. https://doi.org/10.1016/j.colsurfa.2009.05.022

[63]. Yang, W., Li, X., Pan, B., Lv, L., & Zhang, W. (2013). Effective removal of effluent organic matter (EfOM) from bio-treated coking wastewater by a recyclable aminated hyper-cross-linked polymer. Water Research, 47(13), 4730–4738. https://doi.org/10.1016/j.watres.2013.05.032

[64]. Xu, C., Wang, C., Sun, W., Yu, W., Yin, C., Liu, F., Xian, M., & Yu, S. (2019). Preparation of hypercrosslinked amine modification resin and its adsorption properties for nitroaromatics. Environmental Science and Pollution Research, 26(11), 10767–10775. https://doi.org/10.1007/s11356-019-04370-4

[65]. Santos, D. P. D., Andrade, G. F. S., Temperini, M. L. A., & Brolo, A. G. (2009). Electrochemical Control of the Time-Dependent Intensity Fluctuations in Surface-Enhanced Raman Scattering (SERS). The Journal of Physical Chemistry C, 113(41), 17737–17744. https://doi.org/10.1021/jp907389v

[66]. Ramírez-Herrera, C. A., Cruz-Cruz, I., Jiménez-Cedeño, I. H., Martínez-Romero, O., & Elías-Zúñiga, A. (2021). Influence of the epoxy resin process parameters on the mechanical properties of produced bidirectional [±45°] Carbon/Epoxy woven composites. Polymers, 13(8), 1273. https://doi.org/10.3390/polym13081273

[67]. Sarno, M., Iuliano, M., De Pasquale, S., & Ponticorvo, E. (2020). A new nano-catalyst for sawdust hydrolysis. Applied Catalysis A: General, 602, 117686. https://doi.org/10.1016/j.apcata.2020.117686

[68]. Wang, J., Yue, D., & Wang, H. (2020). In situ Fe_3O_4 nanoparticles coating of polymers for separating hazardous PVC

from microplastic mixtures. Chemical Engineering Journal, 407, 127170. https://doi.org/10.1016/j.cej.2020.127170

[69]. Peng, Q., Zhao, H., Chen, G., Yang, Q., Cao, X., Xiong, S., Xiao, A., Li, G., Liu, B., & Liu, Q. (2023). Synthesis of novel magnetic pitch-based hypercrosslinked polymers as adsorbents for effective recovery of Ag+ with high selectivity. Journal of Environmental Management, 339, 117763. https://doi.org/10.1016/j.jenvman.2023.117763

[70]. Modestino, M., Galluzzi, A., Sarno, M., & Polichetti, M. (2023). The effect of a DC magnetic field on the AC magnetic properties of oleic acid-coated Fe_3O_4 nanoparticles. Materials, 16(12), 4246. https://doi.org/10.3390/ma16124246

[71]. Mørup, S., Frandsen, C., & Hansen, M. F. (2010). Magnetic properties of nanoparticles. International Journal of Modern Physics B, 1. Oxford University Press.

[72]. Modestino, M., Galluzzi, A., Sarno, M., & Polichetti, M. (2023). Study of the coercivity field in a sample of $NiFe_2O_4$–OA nanoparticles at different temperatures: Comparing the different processes to evaluate TB by DC measurements. IEEE Nanotechnology Materials and Devices Conference, 259–263. https://doi.org/10.1109/nmdc57951.2023.10343818

[73]. Modestino, M., Galluzzi, A., Barozzi, M., Copelli, S., Daniele, F., Russo, E., Sieni, E., Sgarbossa, P., Lamberti, P., & Polichetti, M. (2025). The effect of copper adsorption on iron oxide magnetic nanoparticles embedded in a sodium alginate bead.

Nanomaterials, 15(15), 1196. https://doi.org/10.3390/nano15151196

[74]. Bruvera, I. J., Zélis, P. M., Calatayud, M. P., Goya, G. F., & Sánchez, F. H. (2015). Determination of the blocking temperature of magnetic nanoparticles: The good, the bad, and the ugly. Journal of Applied Physics, 118(18). https://doi.org/10.1063/1.4935484

[75]. Micha, J., Dieny, B., Régnard, J., Jacquot, J., & Sort, J. (2004). Estimation of the Co nanoparticles size by magnetic measurements in Co/SiO_2 discontinuous multilayers. Journal of Magnetism and Magnetic Materials, 272–276, E967–E968. https://doi.org/10.1016/j.jmmm.2003.12.268

[76]. Iuliano, M., Ponticorvo, E., Cirillo, C., Adami, R., & Sarno, M. (2023). Catalytic hydrogenation of organic dyes by Ag and Au magnetic nanoparticles supported on nanocellulose from waste pistachio shells. Molecular Catalysis, 544, 113179. https://doi.org/10.1016/j.mcat.2023.113179

[77]. Iuliano, M., Cirillo, C., Astorga, E. N., & Sarno, M. (2024). A new nanocomposite as adsorbent and catalyst for enhanced removal of methylene blue. Surfaces and Interfaces, 51, 104582. https://doi.org/10.1016/j.surfin.2024.104582

[78]. Azim, E. A., Samy, M., Hanafy, M., & Mahanna, H. (2024). Novel mint-stalks derived biochar for the adsorption of methylene blue dye: Effect of operating parameters, adsorption mechanism, kinetics, isotherms, and thermodynamics. Journal of Environmental Management, 357, 120738. https://doi.org/10.1016/j.jenvman.2024.120738

[79]. Tran, T. H., Le, H. H., Pham, T. H., Nguyen, D. T., La, D. D., Chang, S. W., Lee, S. M., Chung, W. J., & Nguyen, D. D. (2021). Comparative study on methylene blue adsorption behavior of coffee husk-derived activated carbon materials prepared using hydrothermal and soaking methods. Journal of Environmental Chemical Engineering, 9(4), 105362. https://doi.org/10.1016/j.jece.2021.105362

[80]. Tran, T. H., Le, A. H., Pham, T. H., Nguyen, D. T., Chang, S. W., Chung, W. J., & Nguyen, D. D. (2020). Adsorption isotherms and kinetic modeling of methylene blue dye onto a carbonaceous hydrochar adsorbent derived from coffee husk waste. The Science of the Total Environment, 725, 138325. https://doi.org/10.1016/j.scitotenv.2020.138325

[81]. Afroze, S., Sen, T. K., Ang, M., & Nishioka, H. (2015). Adsorption of methylene blue dye from aqueous solution by novel biomass Eucalyptus sheathiana bark: equilibrium, kinetics, thermodynamics and mechanism. Desalination and Water Treatment, 57(13), 5858–5878. https://doi.org/10.1080/19443994.2015.1004115

[82]. Shu, J., Liu, R., Wu, H., Liu, Z., Sun, X., & Tao, C. (2017). Adsorption of methylene blue on modified electrolytic manganese residue: Kinetics, isotherm, thermodynamics and mechanism analysis. Journal of the Taiwan Institute of Chemical Engineers, 82, 351–359. https://doi.org/10.1016/j.jtice.2017.11.020

[83]. Nipa, S. T., Shefa, N. R., Parvin, S., Khatun, M. A., Alam, M. J., Chowdhury, S., Khan, M. a. R., Shawon, S. M. a. Z., Biswas, B.

K., & Rahman, M. W. (2022). Adsorption of methylene blue on papaya bark fiber: Equilibrium, isotherm and kinetic perspectives. Results in Engineering, 17, 100857. https://doi.org/10.1016/j.rineng.2022.100857

[84]. El-Bendary, N., El-Etriby, H. K., & Mahanna, H. (2021). High-performance removal of iron from aqueous solution using modified activated carbon prepared from corn cobs and luffa sponge. Desalination and Water Treatment, 213, 348–357. https://doi.org/10.5004/dwt.2021.26721

[85]. Duran, C., Özdeş, D., Gündoğdu, A., & Şentürk, H. B. (2011). Kinetics and Isotherm Analysis of Basic Dyes Adsorption onto Almond Shell (Prunus dulcis) as a Low Cost Adsorbent. Journal of Chemical and Engineering Data/Journal of Chemical & Engineering Data, 56(5), 2136–2147. https://doi.org/10.1021/je101204j

[86]. Fu, J., Chen, Z., Wang, M., Liu, S., Zhang, J., Zhang, J., Han, R., & Xu, Q. (2014). Adsorption of methylene blue by a high-efficiency adsorbent (polydopamine microspheres): Kinetics, isotherm, thermodynamics and mechanism analysis. Chemical Engineering Journal, 259, 53–61. https://doi.org/10.1016/j.cej.2014.07.101

[87]. Farch, S., Yahoum, M. M., Toumi, S., Tahraoui, H., Lefnaoui, S., Kebir, M., Zamouche, M., Amrane, A., Zhang, J., Hadadi, A., & Mouni, L. (2023). Application of walnut shell biowaste as an inexpensive adsorbent for methylene blue dye: isotherms, kinetics,

thermodynamics, and modeling. Separations, 10(1), 60. https://doi.org/10.3390/separations10010060

[88]. Yuan, W., Zhou, L., Zhang, Z., Ying, Y., Fan, W., Chai, K., Zhao, Z., Tan, Z., Shen, F., & Ji, H. (2021). Synergistic dual-functionalities of starch-grafted-styrene hydrophilic porous resin for efficiently removing bisphenols from wastewater. Chemical Engineering Journal, 429, 132350. https://doi.org/10.1016/j.cej.2021.132350

[89]. Alver, E., & Metin, A. Ü. (2012). Anionic dye removal from aqueous solutions using modified zeolite: Adsorption kinetics and isotherm studies. Chemical Engineering Journal, 200–202, 59–67. https://doi.org/10.1016/j.cej.2012.06.038

[90]. Melo, B. C., Paulino, F. A., Cardoso, V. A., Pereira, A. G., Fajardo, A. R., & Rodrigues, F. H. (2017). Cellulose nanowhiskers improve the methylene blue adsorption capacity of chitosan-g-poly(acrylic acid) hydrogel. Carbohydrate Polymers, 181, 358–367. https://doi.org/10.1016/j.carbpol.2017.10.079

[91]. Long, Z., Wang, Z., Huang, Q., Jia, Y., Jiao, Z., Wang, Y., & Du, Y. (2024). High-performance adsorption of methylene blue using novel bio-adsorbent based on sargassum fusiforme. Heliyon, 10(18), e37949. https://doi.org/10.1016/j.heliyon.2024.e37949

[92]. Huang, D., Xu, B., Tang, J., Luo, J., Chen, L., Yang, L., Yang, Z., & Bi, S. (2009). Indirect determination of sulfide ions in water samples at trace level by anodic stripping voltammetry using mercury film electrode. Analytical Methods, 2(2), 154–158. https://doi.org/10.1039/b9ay00183b

[93]. Nasar, A., & Mashkoor, F. (2019). Application of polyaniline-based adsorbents for dye removal from water and wastewater—a review. Environmental Science and Pollution Research, 26(6), 5333–5356. https://doi.org/10.1007/s11356-018-3990-y

[94]. Xing, Y., Shen, X., Niu, Q., Duan, H., Tang, C., Tao, B., Chen, S., Shangguan, Q., Feng, B., Yu, H., Tang, Z., & Ji, G. (2025). Thermally and chemically stable Fe/Mg-layered double oxides-biochar for enhanced polystyrene nanoplastic adsorption and sustainable recycling. Chemical Engineering Journal, 508, 160918. https://doi.org/10.1016/j.cej.2025.160918

[95]. Wang, P., Cao, M., Wang, C., Ao, Y., Hou, J., Qian, J., 2014. Kinetics and thermodynamics of adsorption of methylene blue by a magnetic graphene-carbon nanotube composite. Appl. Surf. Sci. 290, 116e124.

[96]. Allou, N. B., Tigori, M. A., Koffi, A. A., Halidou, M., Eroi, N. S., Atheba, P., & Trokourey, A. (2023b). Methylene blue magnetic adsorption separation process from aqueous solution using corn cob. Scientific African, 21, e01828. https://doi.org/10.1016/j.sciaf.2023.e01828

[97]. Gong, J., Wang, B., Zeng, G., Yang, C., Niu, C., Niu, Q., Zhou, W., & Liang, Y. (2008). Removal of cationic dyes from aqueous solution using magnetic multi-wall carbon nanotube nanocomposite as adsorbent. Journal of Hazardous Materials, 164(2–3), 1517–1522. https://doi.org/10.1016/j.jhazmat.2008.09.072

[98]. Ge, Y., Zhang, Y., Yang, Y., Xie, S., Liu, Y., Maruyama, T., Deng, Z., & Zhao, X. (2019). Enhanced adsorption and catalytic degradation of organic dyes by nanometer iron oxide anchored to single-wall carbon nanotubes. Applied Surface Science, 488, 813–826. https://doi.org/10.1016/j.apsusc.2019.05.221

[99]. Ahamad, T., Naushad, M., Eldesoky, G. E., Al-Saeedi, S. I., Nafady, A., Al-Kadhi, N. S., Al-Muhtaseb, A. H., Khan, A. A., & Khan, A. (2019). Effective and fast adsorptive removal of toxic cationic dye (MB) from aqueous medium using amino-functionalized magnetic multiwall carbon nanotubes. Journal of Molecular Liquids, 282, 154–161. https://doi.org/10.1016/j.molliq.2019.02.128

[100]. Foroutan, R., Mohammadi, R., Razeghi, J., & Ramavandi, B. (2019). Performance of algal activated carbon/Fe3O4 magnetic composite for cationic dyes removal from aqueous solutions. Algal Research, 40, 101509. https://doi.org/10.1016/j.algal.2019.101509

Table 1. Comparative adsorption performance of Fe_3O_4@XDV-NH_2 nanocomposites and other magnetic adsorbent materials for methylene blue removal.

Adsorbents	Adsorption capacity (mg/g)	Reusability	Reference
MGC-4	65.79	4 cycles (Decreased slightly)	[95]
Magnetized corn cob	13.23	5 cycles (stay above 68 %)	[96]
Magnetic multi-wall carbon nanotube	48.06	-	[97]
AO-Fe-SWCNTs	256.69	4 cycles (Stay above 55%)	[98]
NH_2-MWCNTs@Fe_3O_4	178.5	6 cycles (Stay above 80%)	[99]
ACSO/Fe_3O_4	60.60	7 cycles (Decrease by 3%)	[100]
Fe_3O_4@XDV-NH_2.	79.60	6 cycles (Stay above 89%)	This work

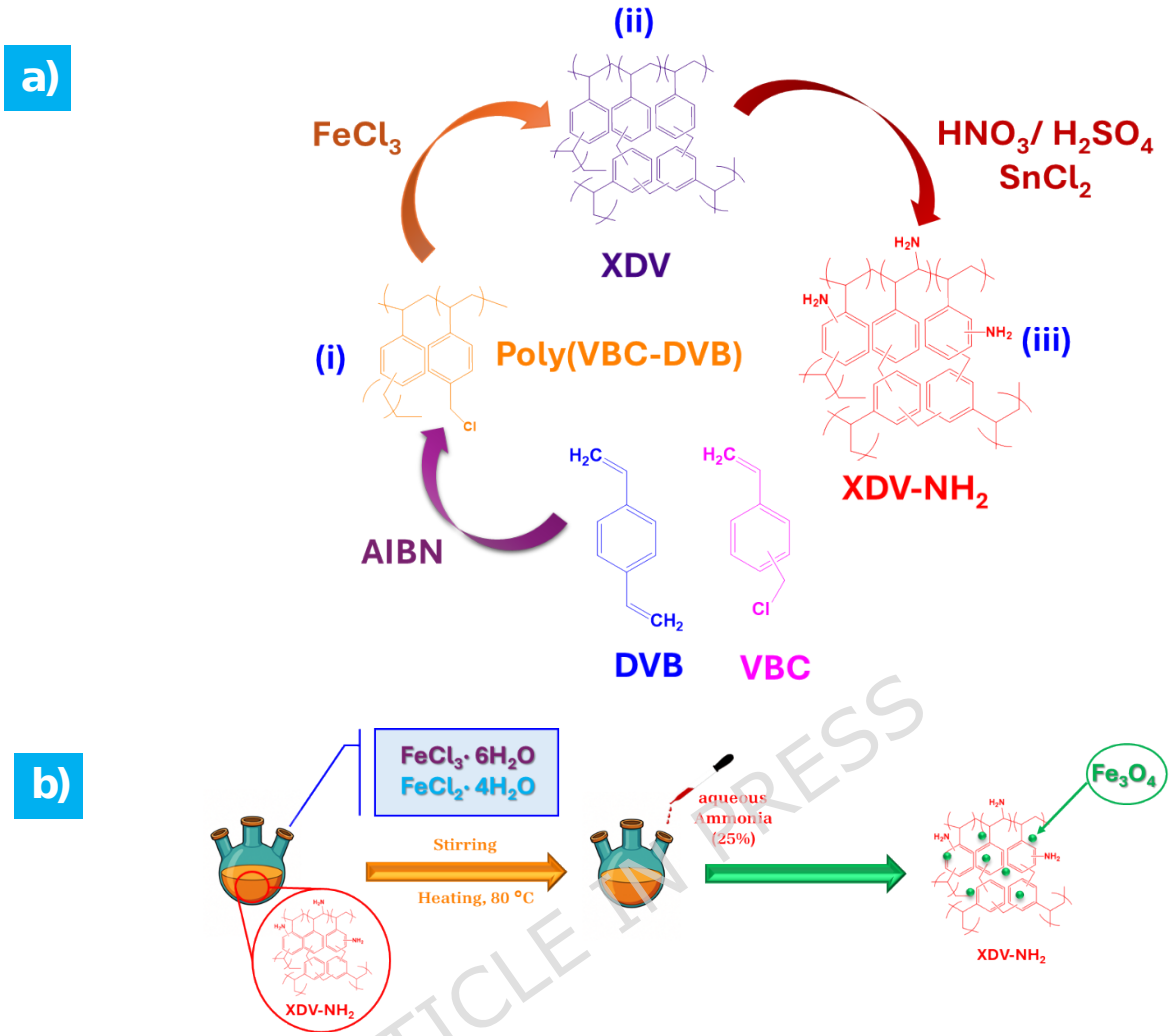

Figure 1. Schematic illustration of amino-functionalized hyper-crosslinked resin (XDV-NH_2) synthesis (a), and precipitation of iron oxide nanoparticles (Fe_3O_4 NPs) in amino-functionalized hyper-crosslinked resin (XDV-NH_2) (b).

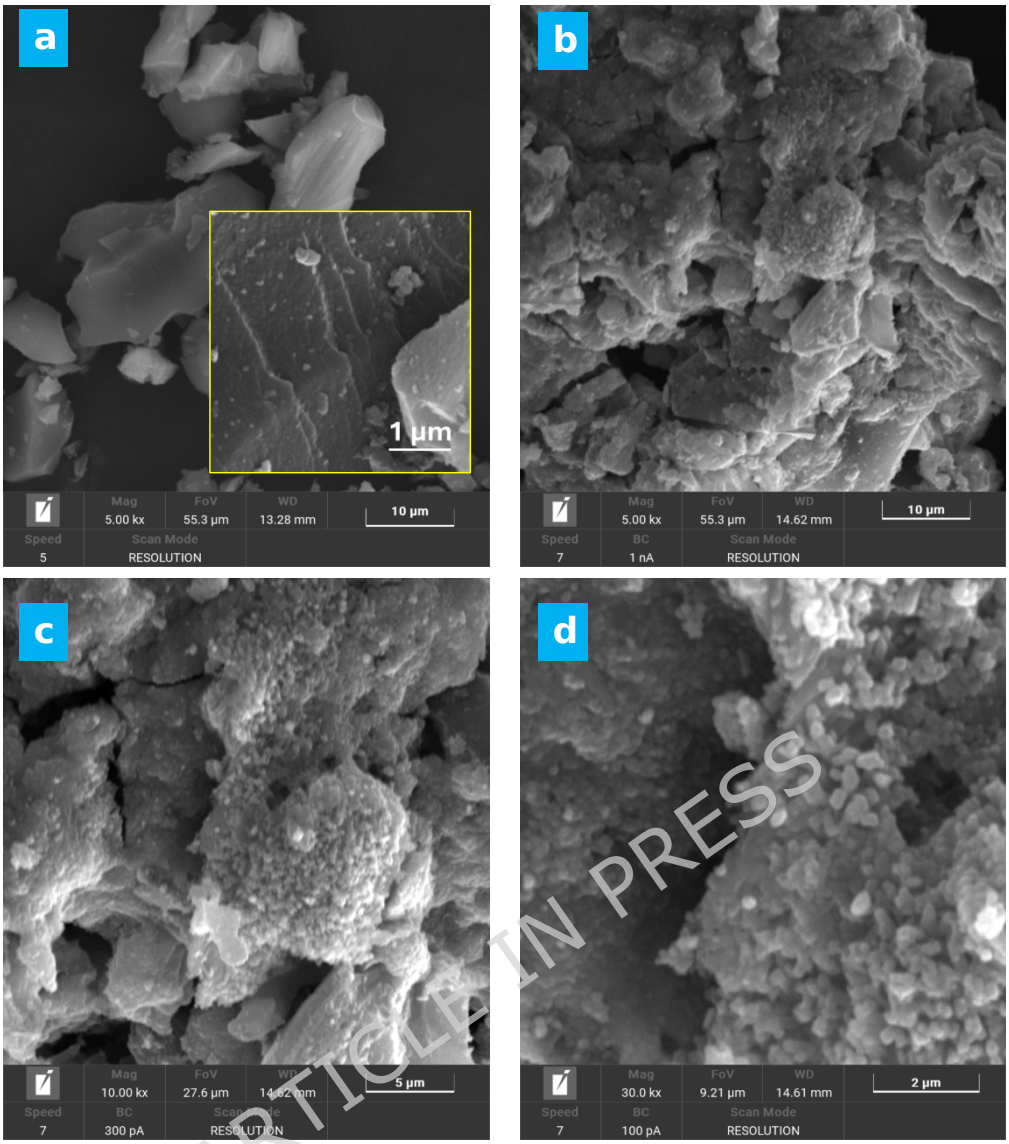

Figure 2. Scanning electron microscopy (SEM) analysis of amino-functionalized hyper cross-linked resin (XDV-NH_2) (a); high resolution of XDV-NH_2 (inset a), and magnetic amino-hyper cross-linked (Fe_3O_4@XDV-NH_2) (b-d) at different magnifications.

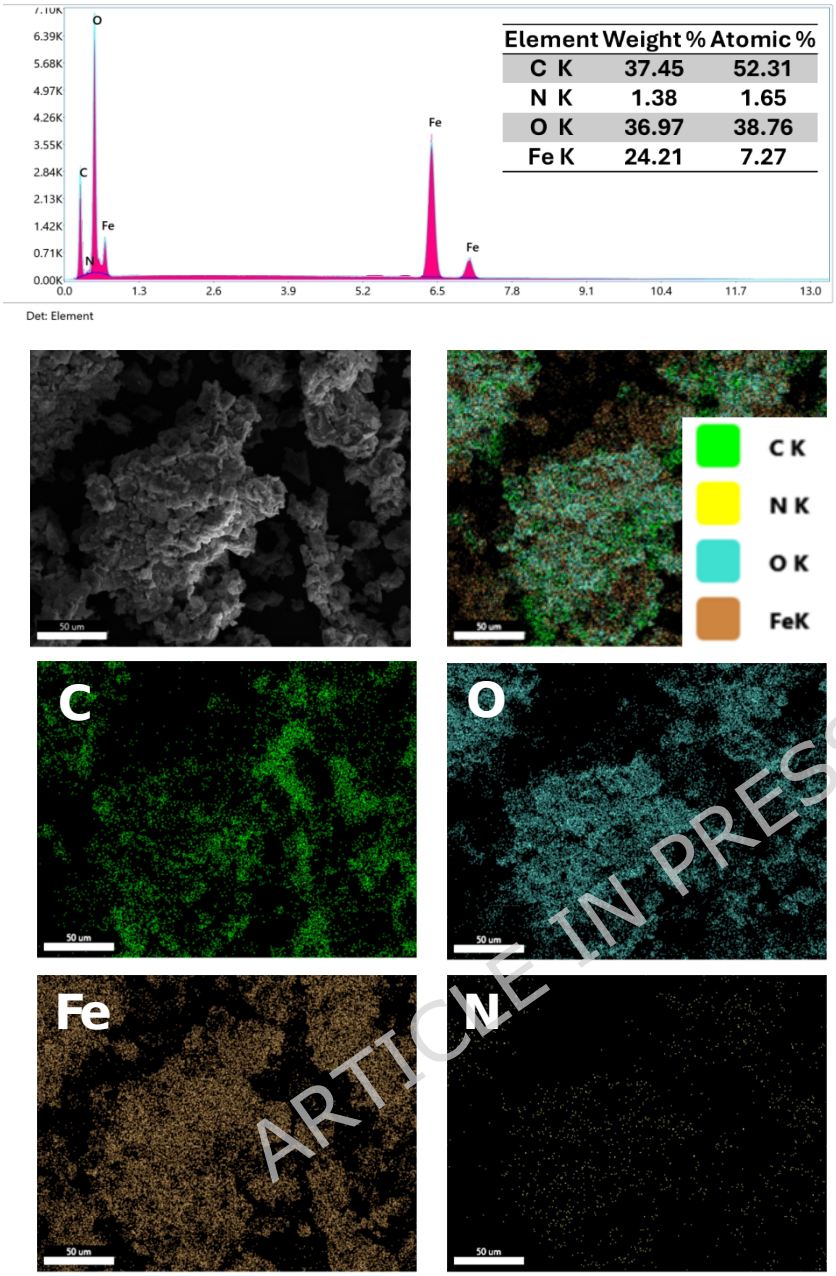

Figure 3. Energy-dispersive X-ray spectroscopy (EDX) spectrum of magnetic amino-hyper-cross-linked (Fe_3O_4@XDV-NH_2) for C, Fe, N, and O elements (a,b).

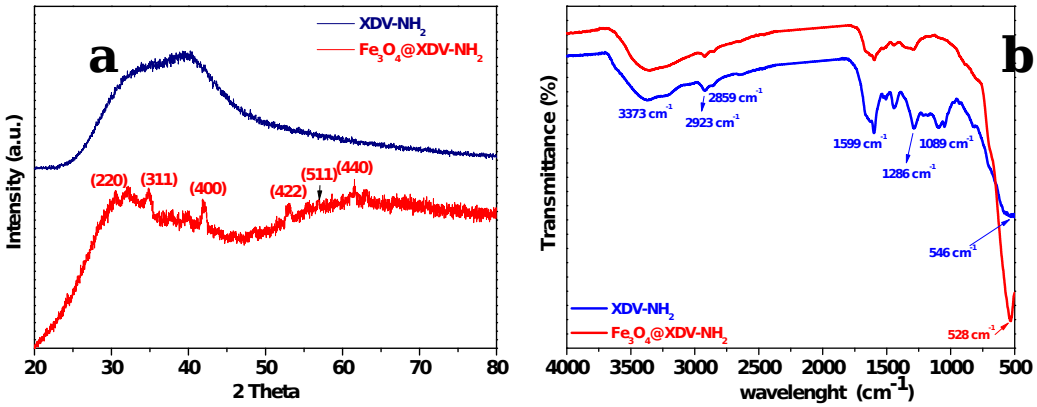

Figure 4. X-Ray diffraction (XRD) profile of amino-hyper cross-linked resin (XDV-NH_2) and magnetic amino-hyper cross-linked resin (Fe_3O_4@XDV-NH_2) in the range 2θ: 20°-80° (a); Fourier-transform infrared spectra (FT-IR) in the range of wavenumber 4000-500 cm^{-1} of amino-functionalized hyper cross-linked resin (XDV-NH_2), magnetic amino-hyper cross-linked resin (Fe_3O_4@XDV-NH_2) (b).

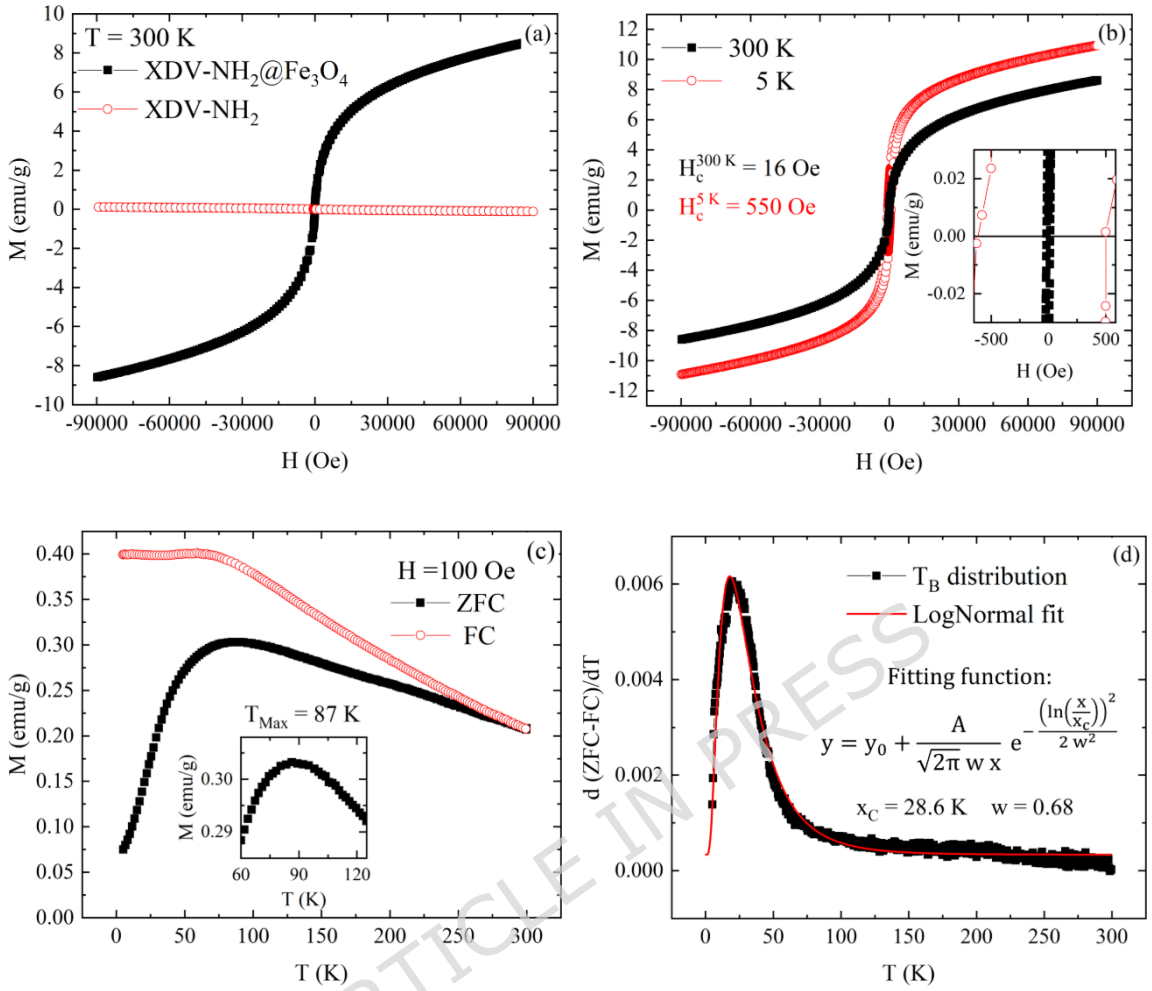

Figure 5. (a) Comparison of M(H) measurements at 300 K for the sample of XVD-NH_2 with (black) and without (red) the magnetic nanoparticles embedded. (b) Comparison of M(H) measurements at 5K (in red) and 300 K (in black) for the XDV- $NH_2@Fe_3O_4$ sample. In the inset, it is possible to observe the detail around the zero field. From this, the coercive field at the two temperatures has been evaluated as 550 Oe at 5 K and 16 Oe at 300 K; (c) M(T) measurement in the range between 5 K and 300 K under an applied field of 100 Oe. The ZFC curve and the FC curve are plotted respectively in black and red. In the inset, the maximum of the ZFC curve is shown at 87 K. The blocking temperature distribution obtained by the M(T) measurement in Figure 5(c).(d) The curve follows the lognormal distribution as expected for a sample of magnetic nanoparticles.

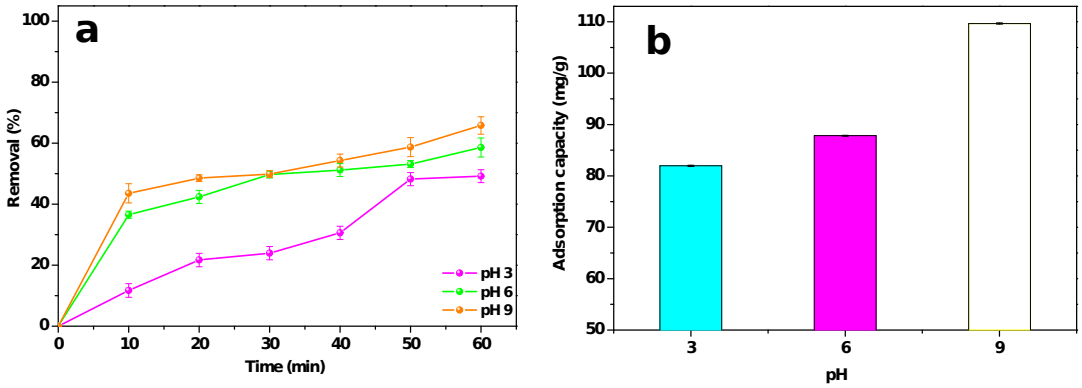

Figure 6. Effect of pH, as a function of time, on the kinetics of adsorption of methylene blue (MB) (a) and on the adsorption capacity of MB (b). Adsorption conditions: Fe_3O_4@XDV-NH_2 = 0.03 g/L; initial MB concentration = 5 mg/L; T = 25 °C and agitation speed=220 rpm. Each data point represents the mean of three independent measurements (n = 3), and the error bars correspond to the standard error of the mean

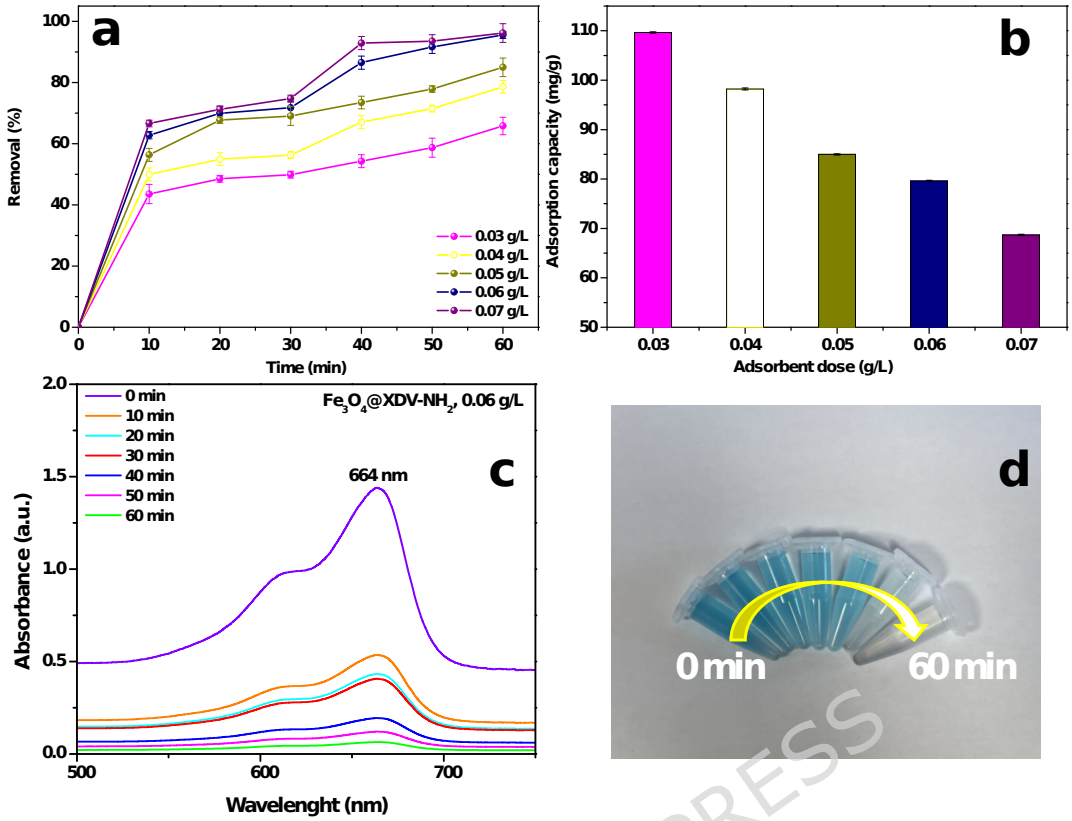

Figure 7. Effect of adsorbent dosage, on the time-dependent adsorption efficiency of methylene blue (MB) (a) and on the adsorption capacity of MB (b); UV–vis spectra of MB removal with 0.06 g/L adsorbent as a function of time (c); photograph of MB color change over time (d). Adsorption conditions: pH = 9; initial MB concentration = 5 mg/L; T = 25 °C; and agitation speed = 220 rpm. Each data point represents the mean of three independent measurements (n = 3), and the error bars correspond to the standard error of the mean

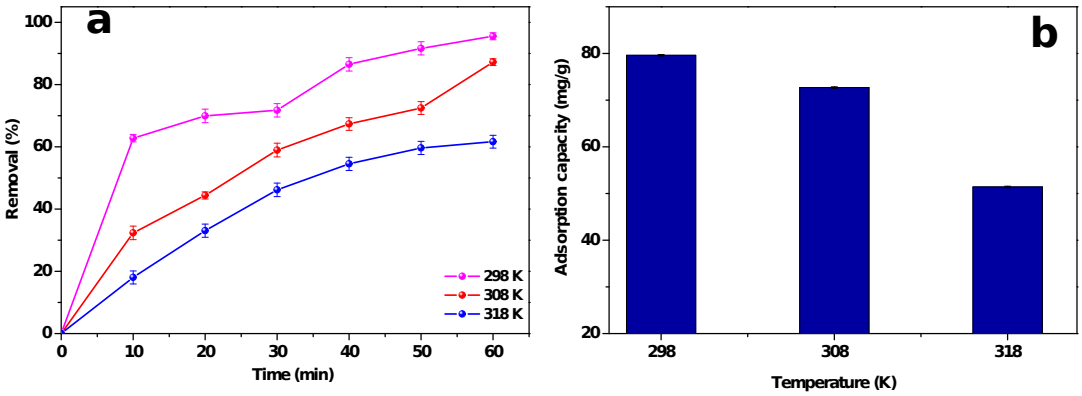

Figure 8. Effect of temperature on the time-dependent adsorption efficiency of methylene blue (MB) (a) and on the adsorption capacity of MB (b). Adsorption conditions: pH = 9; initial MB concentration = 5 mg/L; Fe_3O_4@XDV-NH_2 = 0.06 g/L; and agitation speed = 220 rpm. Each data point represents the mean of three independent measurements (n = 3), and the error bars correspond to the standard error of the mean.

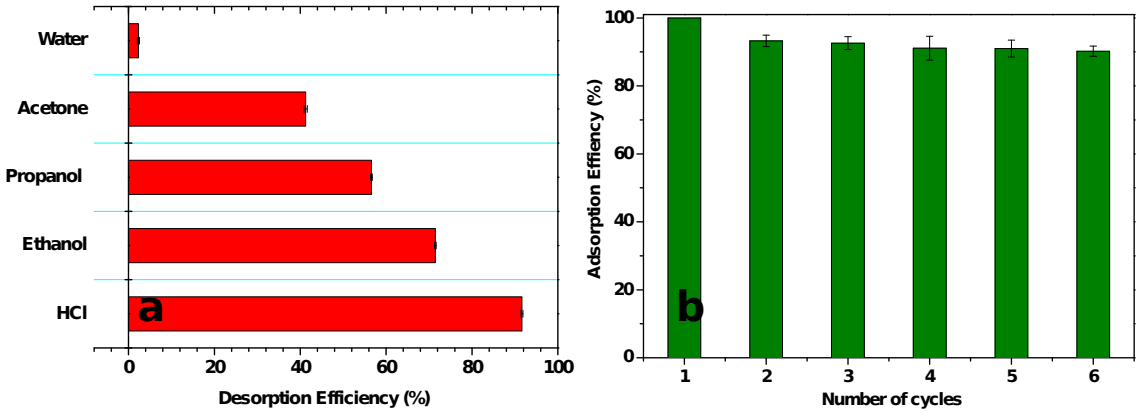

Figure 9. Desorption efficiency of MB using different solvents, Desorption condition (Solvent; contact time 120 min; T = 25 °C) (a). Reusability of Fe_3O_4@XDV-NH_2. Adsorption conditions: pH = 9; adsorption dose: 0.06 g/L; initial MB concentration = 5 mg/L; T = 25 °C; and agitation speed = 220 rpm. Desorption condition (HCl; contact time 120 min; T = 25 °C) (b). Each data point represents the mean of three independent measurements (n = 3), and the error bars correspond to the standard error of the mean